REPRODUCTIVE BIOLOGY

Temperature-activated ion channels in neural crest cells confer maternal fever–associated birth defects

Mary R. Hutson,[1]* Anna L. Keyte,[1,2,3]* Miriam Hernández-Morales,[2,3,4,5] Eric Gibbs,[2,3] Zachary A. Kupchinsky,[6] Ioannis Argyridis,[2,3] Kyle N. Erwin,[1] Kelly Pegram,[1] Margaret Kneifel,[2,3] Paul B. Rosenberg,[7] Pavle Matak,[8] Luke Xie,[2,3] Jörg Grandl,[9] Erica E. Davis,[6] Nicholas Katsanis,[6] Chunlei Liu,[2,3,4,5]† Eric J. Benner[1]†

Birth defects of the heart and face are common, and most have no known genetic cause, suggesting a role for environmental factors. Maternal fever during the first trimester is an environmental risk factor linked to these defects. Neural crest cells are precursor populations essential to the development of both at-risk tissues. We report that two heat-activated transient receptor potential (TRP) ion channels, TRPV1 and TRPV4, were present in neural crest cells during critical windows of heart and face development. TRPV1 antagonists protected against the development of hyperthermia-induced defects in chick embryos. Treatment with chemical agonists of TRPV1 or TRPV4 replicated hyperthermia-induced birth defects in chick and zebrafish embryos. To test whether transient TRPV channel permeability in neural crest cells was sufficient to induce these defects, we engineered iron-binding modifications to TRPV1 and TRPV4 that enabled remote and noninvasive activation of these channels in specific cellular locations and at specific developmental times in chick embryos with radio-frequency electromagnetic fields. Transient stimulation of radio frequency–controlled TRP channels in neural crest cells replicated fever-associated defects in developing chick embryos. Our data provide a previously undescribed mechanism for congenital defects, whereby hyperthermia activates ion channels that negatively affect fetal development.

INTRODUCTION

Birth defects of the heart and face are extremely common. Congenital heart defects affect about 1% of live births in the United States and often require surgical correction within the first year of life (1). Craniofacial clefts involving the lip and/or the palate affect more than 4000 infants per year and typically require corrective surgery (2). Genetic associations have been identified in only 15% of heart defects or 30% of craniofacial defects, leaving most cases without a known etiology (3, 4). Environmental factors likely contribute to these cases. First-trimester maternal fever is an environmental factor linked to both craniofacial and heart defects (5). Highly associated heart defects include right- and left-sided obstructive lesions (pulmonary atresia, pulmonary stenosis, and aortic stenosis) and conotruncal defects [double outlet right ventricle (DORV) and tetralogy of Fallot] (6–8). Hyperthermia-associated craniofacial defects include midface hypoplasia and cleft lip and/or palate (5, 9). Specific modes of infections, such as respiratory infections compared to urinary or pelvic infections, confer differential susceptibilities, leading some to speculate that infection itself is the critical event (7, 8). However, maternal hyperthermia after hot tub exposure is sufficient to confer risk of birth defects, suggesting that hyperthermia itself is the principal ter-

atogen (10). Nonetheless, the teratogenic mechanisms of maternal fever are unknown.

Craniofacial clefts, abnormal arch artery anatomy, aorticopulmonary septation, and conotruncal heart defects can be linked through neural crest cell dysfunction (11, 12). Neural crest cells are a pluripotent migratory cell population that arises from the dorsal neural tube. Cranial and cardiac neural crest cells migrate to the head and pharyngeal arches where they contribute to the developing face and heart. The cranial neural crest cells differentiate into the bone and cartilage that form facial features including the jaw and palate (13). The cardiac neural crest cells are required for septation of the aorta and pulmonary trunk (11). In addition, they differentiate into the smooth muscle cells of the aortic arch arteries, the distal aorta, and the pulmonary trunk and are required for aortic arch patterning (14). Further, neural crest cells influence early cardiac function and the development of the secondary heart field, a cardiogenic cell population in the pharynx required for proper alignment of the outflow vessels with respect to the ventricles (15–17). Therefore, fever-induced changes to neural crest cell function could provide a unifying mechanism to account for the types of birth defects observed after fever.

During our investigation, we discovered that two temperature-activated transient receptor potential (TRP) ion channels, TRPV1 and TRPV4, are present in cardiac and cranial neural crest cells during critical windows of heart and facial development. Several TRP channels are the principal components for temperature sensation within sensory neurons (18–20), although other TRP channel functions include modulating Ca^{2+} during cytoskeleton rearrangements, promoting cell polarity critical for cell migration, and regulation of cellular metabolism, suggesting highly diverse functions outside the nervous system (21–23). We hypothesized that transient changes in the activity of temperature-activated TRP channels in neural crest cells confer susceptibility to fever-associated craniofacial and congenital heart defects. Using pharmacological approaches to antagonize TRP activity, we protected developing chick embryos from hyperthermia-mediated

[1]Division of Neonatology, Department of Pediatrics, Duke University Medical Center, Jean and George Brumley, Jr. Neonatal-Perinatal Institute, Durham, NC 27710, USA. [2]Brain Imaging and Analysis Center, Duke University School of Medicine, Durham, NC 27710, USA. [3]Department of Radiology, Duke University School of Medicine, Durham, NC 27710, USA. [4]Department of Electrical Engineering and Computer Sciences, University of California, Berkeley, CA 94720, USA. [5]Helen Wills Neuroscience Institute, University of California, Berkeley, CA 94720, USA. [6]Center for Human Disease Modeling, Duke University Medical Center, Durham, NC 27710, USA. [7]Department of Medicine, Duke University School of Medicine, Durham, NC 27710, USA. [8]Department of Pharmacology and Cancer Biology, Duke University School of Medicine, Durham, NC 27710, USA. [9]Department of Neurobiology, Duke University Medical Center, Durham, NC 27710, USA.
*These authors contributed equally to this work.
†Corresponding author. Email: eric.benner@duke.edu (E.J.B); chunlei.liu@berkeley.edu (C.L.)

birth defects. In addition, we used a TRP channel agonist to replicate associated birth defects under normothermic conditions. Finally, we developed a technology to remotely control transient permeability of temperature-activated TRP channels with cellular resolution using radio-frequency (RF) waves. Transient activation of these TRP channels in neural crest cells was sufficient to replicate febrile-associated birth defects.

RESULTS

Hyperthermia induced neural crest cell–related birth defects

We investigated the developmental effects of hyperthermia on neural crest cell–derived craniofacial and cardiovascular structures in chick embryos. The mechanisms of neural crest cell development are largely conserved between species, and chick is a well-established model to study human cardiovascular and craniofacial defects. To target critical stages in neural crest cell development, we heated Hamburger Hamilton stage 11 (HH11) to HH15 embryos at 40° to 41°C for 1 hour, reincubated them at 37°C, and then analyzed them for craniofacial and heart defects at HH36. We performed alcian blue and alizarin red staining to analyze the craniofacial features in experimental animals (Fig. 1A). Individual upper beak lengths were measured and normalized to femur lengths to account for small variations in staging (Fig. 1B). Our analysis revealed that hyperthermia exposure resulted in significant craniofacial defects, including a reduction in upper beak lengths compared to normothermic control chicks with severe beak defects observed in 16% of hyperthermia-exposed animals (Fig. 1C and fig. S1, A and B). Cardiovascular defects were increased in hyperthermia-exposed embryos. These defects included a significant incidence of conotruncal defects including DORV (Fig. 1, D and E) and aortic arch patterning defects (fig. S2, A to F). All of these defects are directly linked to neural crest cell dysfunction (12). Because of the high association of outflow tract obstruction defects with maternal fevers in humans, we used stereology to analyze the luminal cross-sectional areas of the aorta and pulmonary trunk using the Cavalieri probe (24). We identified a 72 and 55% reduction in luminal cross-sectional areas of the aorta and pulmonary trunk, respectively (Fig. 1, F and G). The obstructive lesions were supravalvular and coincident with neural crest–derived smooth muscle vessel regions. These data demonstrate that experimentally controlled hyperthermia in chick models can produce neural crest–associated birth defects reminiscent of those observed in human infants after maternal fever.

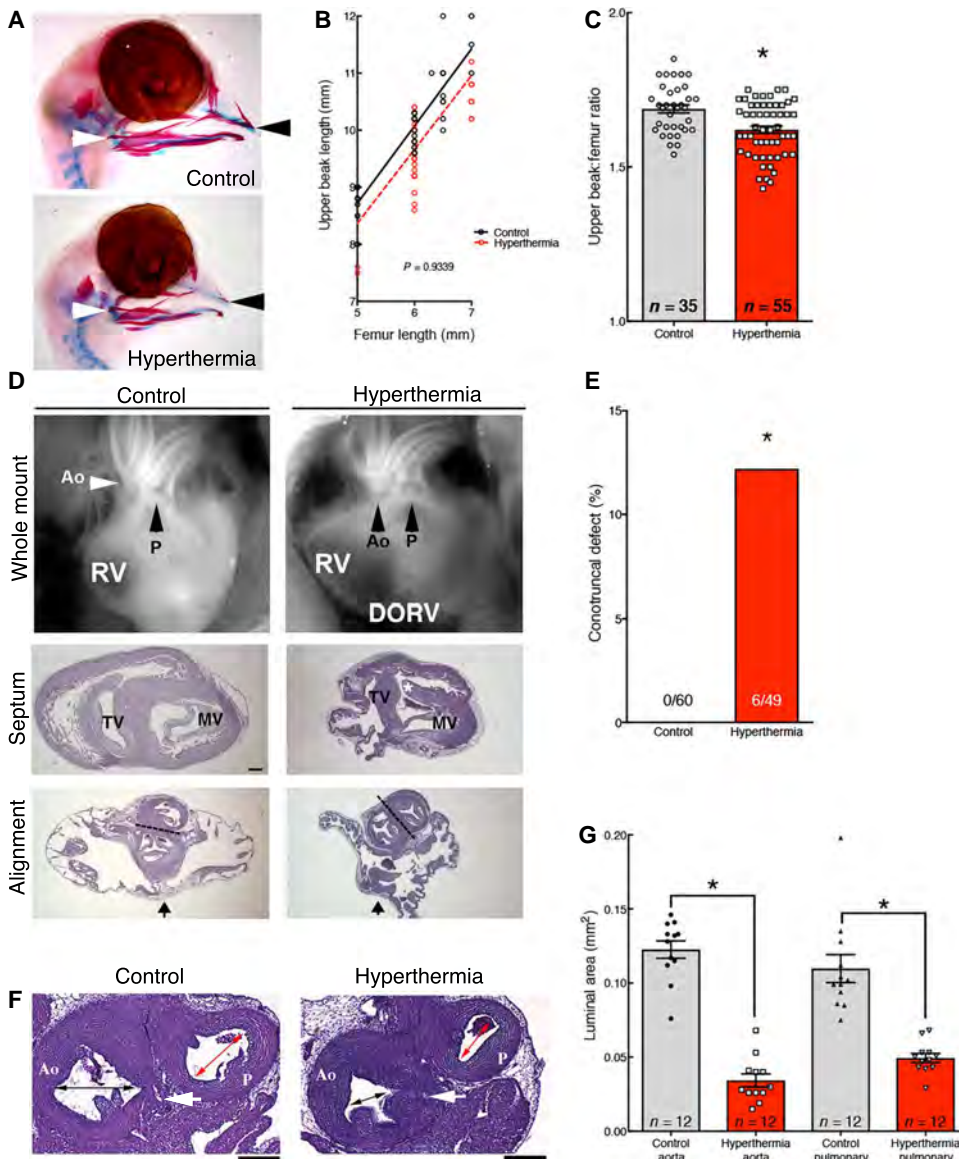### TRPV1 channel inhibition mitigated fever-associated birth defects

To identify potential teratogenic mechanisms of hyperthermia, we first examined the expression profile of mRNAs encoding temperature-activated vanilloid TRP channels (TRPV1 to TRPV4) in neural folds containing neural crest cells in chick embryos at HH9 using reverse transcription polymerase chain reaction (RT-PCR). As a control, mRNA transcripts for all four TRPV channels were detected in whole-embryo RNA from HH14 and HH22-to-HH24 embryos. However, only transcripts for TRPV1, TRPV2, and TRPV4 were detected in dissected neural folds enriched for premigratory neural crest cells at HH9 (fig. S3A). TRPV2 is activated by temperatures >52°C, thus making this channel less likely to be affected by temperatures experienced during fever (19). However, TRPV1 and TRPV4 can mediate heat-evoked Ca²⁺ currents >40° and >34°C, respectively, making these likely candidates for fever-induced activation (18, 25). To verify the ex-

pression of TRPV1 and TRPV4 in migrating neural crest cells, we electroporated neural tubes with a plasmid encoding green fluorescent protein (GFP) at HH9, explanted them, and cultured them overnight to allow for GFP⁺ neural crest cells to migrate from the neural tube (fig. S3B). RT-PCR analysis on FACS (fluorescence-activated cell sorter)–sorted GFP⁺ neural crest cells (fig. S3, C and D) confirmed that both TRPV1 and TRPV4 transcripts were present in this population (fig. S3E).

The neural crest–related defects observed after hyperthermia exposures between HH11 and HH15 suggested a critical developmental window of susceptibility. To determine whether cranial and cardiac neural crest cells expressed TRPV1 and/or TRPV4 during these developmental stages, we combined in situ hybridization for TRPV4 or TRPV1 mRNAs with immunohistochemistry for the neural crest cell marker human natural killer 1 (HNK1). TRPV1 transcripts were detected in HNK1⁺ premigratory and migrating HNK1⁺ cranial and cardiac neural crest cells between HH11 and HH13 (fig. S4, A to J). Similarly, TRPV4 transcripts were also detected at these stages in HNK1⁺ cranial and cardiac neural crest cells (fig. S5, A to F). Thus, both TRPV1 and TRPV4 transcripts are detected in neural crest cells during a critical developmental window of susceptibility to hyperthermia-induced defects. These TRPV1⁺ and TRPV4⁺ neural crest cells populate pharyngeal arches 1 and 2 and are the primary contributors to the bone and cartilage of craniofacial structures. Neural crest cells populating pharyngeal arches 3, 4, and 6 form the outflow septum, the smooth muscle of the great arteries, and influence aortic arch patterning. These neural crest cells are also critical to secondary heart field development and influence conotruncal alignment (17).

Next, we confirmed the responsiveness of chick TRPV1 and TRPV4 with channel-specific ligands. Treatment of chick TRPV4–expressing Chinese hamster ovary (CHO) cells with the TRPV4 agonist, GSK1016790A (hereinafter GSK101), increased Ca²⁺ permeability, as assessed by the genetically encoded Ca²⁺ indicator GCaMP6 (fig. S6A). Identifying an agonist for chick TRPV1 was more challenging because it lacks the capsaicin binding site and is therefore insensitive to capsaicin and related agonists (26). However, the inhibitor cysteine knot (ICK) peptide spider toxin from Psalmopoeus cambridgei, vanilloid toxin 3 (VaTx3), interacts with the outer pore of TRPV1 and is predicted to activate chick TRPV1 (27). VaTx3 produced comparable changes in Ca²⁺ permeability in human embryonic kidney (HEK) 293T cells transiently expressing either the murine or chick TRPV1 channels (fig. S6B). The TRPV1-specific antagonist SB366791 inhibited VaTx3-dependent chick TRPV1 activity (fig. S6C), suggesting that the VaTx3-mediated response was TRPV1-specific.

To determine whether TRPV transcripts detected in neural crest cells translated into functional channels, we electroporated chick neural tubes in ovo at HH9 to HH10 with GCaMP6 and explanted them to culture plates to allow GCaMP6⁺ neural crest cells to migrate from the neural tubes (Fig. 2A). Explanted neural crest cells were exposed to the TRPV4 agonist GSK101, which produced a robust increase in Ca²⁺ permeability that was blocked by pretreatment with the TRPV4 antagonist RN1734 (Fig. 2B) (28). Explanted neural crest cells exposed to VaTx3 showed increased Ca²⁺ responses, demonstrating functional TRPV1 channels in neural crest cells (Fig. 2C). To confirm that neural crest cell–specific TRPV1 and TRPV4 channel activity extended beyond avian species, we analyzed primary mammalian neural crest cells for changes in intracellular Ca²⁺ after exposure to TRPV1 and TRPV4 ligands. Exposing mouse neural crest cell explants to increasing doses of GSK101 produced corresponding increases in Ca²⁺ responses (Fig. 2D), which were blocked by the TRPV4 inhibitor RN1734 (Fig. 2E). Capsaicin

Fig. 1. Hyperthermia-induced congenital defects in neural crest–dependent tissues. (**A**) Alcian blue– and alizarin red–stained craniofacial features of HH36 heads for control and hyperthermia-exposed chicks. Upper beak measurement extended from the quadratojugal (white arrowhead) to the tip of the upper beak (black arrowhead). (**B**) Upper beak length was normalized to femur lengths for control (black) and hyperthermia-exposed (red) chicks. (**C**) Graph of upper beak length–to–femur length ratios for control and hyperthermia chicks. (**D**) Whole-mount and histological sections of HH36 hearts from control (normothermia) and hyperthermia-exposed embryos. The white and black arrowheads in the whole-mount images highlight the alignment of the aorta (Ao) and pulmonary trunk (P) in the control heart compared to the hyperthermia-exposed heart. Histological sections of the whole-mount hearts at the level of the ventricular septum and the outflow vessel semilunar valves. Dashed lines indicate the plane of outflow tract septation. Sections through the hyperthermia-exposed DORV heart with a perimembranous VSD (*) and a rightward shift of the aorta in relation to the pulmonary trunk (dashed line). Gross and histological analysis of heart anatomy was performed in 60 normothermia hearts and 49 hyperthermia-exposed hearts. TV, tricuspid valve; MV, mitral valve. (**E**) Percentage of conotruncal defects in control (0%; $n = 60$ hearts) and hyperthermia groups (12%; $n = 6$ of 49 hearts). (**F**) Representative histological sections through the aorta and the pulmonary trunk used to compare the luminal areas (arrows) of normothermic and hyperthermia-exposed hearts distal to the valves at the level of the left coronary artery (white arrowhead). Scale bars, 200 μm. (**G**) Average Cavalieri probe estimates of the luminal cross-sectional areas of the aorta and pulmonary trunk immediately distal to the respective semilunar valves. Significance was determined using unpaired t test (C and G) or Fisher's exact test (E). *$P <$ 0.0001. The number of biological replicates is indicated by n in the graphs in (C), (E), and (G).

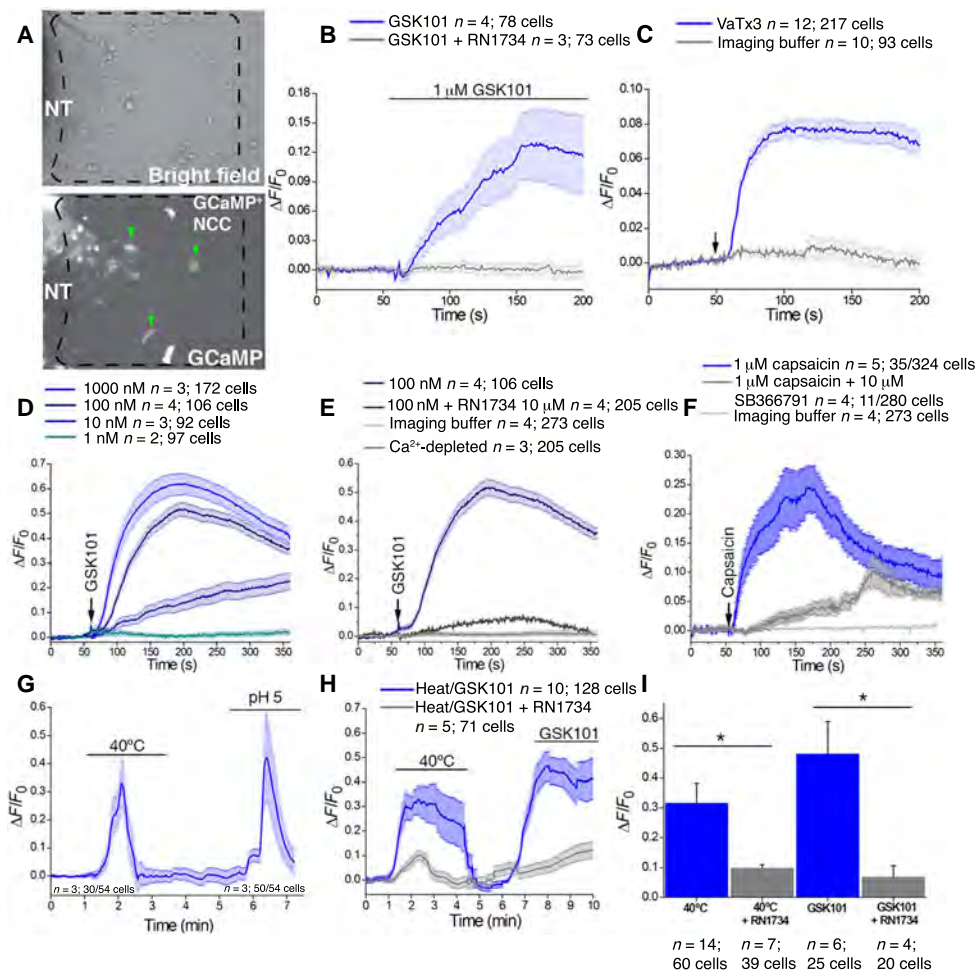application induced Ca^{2+} permeability in mouse neural crest cells, an effect that was blocked by the TRPV1 inhibitor SBB366791 (Fig. 2F). These data demonstrate that TRPV1 and TRPV4 are also present in neural crest cells during mammalian development. Exposure of primary chick neural crest cells to 40°C resulted in increased Ca^{2+} permeability, and this response was reduced by pretreatment with the TRPV4 inhibitor RN1734 (Fig. 2, G to I). Thus, neural crest cells responded to hyperthermia in a manner that was partially mediated through TRPV channels.

We next hypothesized that hyperthermia-induced defects in neural crest–dependent structures in our chick model could be rescued by inhibition of TRPV channels. However, treatment of HH11 embryos with the TRPV4 inhibitor RN1734 under normothermic conditions produced a significant decrease in beak length and a 20% incidence of conotruncal heart defects (fig. S7, A to I). These defects suggested that endogenous TRPV4 activity was necessary for normal craniofacial and heart development, thus precluding us from targeting TRPV4 activity to

rescue hyperthermia-associated birth defects. In contrast, treatment of HH11 embryos with the TRPV1 inhibitor SB366791 treatment at normal temperatures did not produce detectable heart or facial phenotypes. Pretreatment of embryos with SB366791 before hyperthermia prevented hyperthermia-induced craniofacial defects (Fig. 3, A and B) and significantly reduced supravalvular stenosis (Fig. 3, C to E). The number of conotruncal defects was reduced by ~50%, although this trend did not reach statistical significance (fig. S8, A to G). These data link TRPV channel activation with neural crest–related congenital defects in our chick hyperthermia model.

Pharmacological activation of TRPV4 replicated heat-induced birth defects in multiple animal models

As a complementary approach, we exposed developing chick embryos at HH11 to HH15 to the small-molecule TRPV4 agonist GSK101 under normothermic conditions to determine whether pharmacological activation of TRPV4 in ovo induced neural crest–related defects. Conotruncal

We posited that if TRPV activation is a broadly relevant driver mechanism for neural crest–dependent congenital defects, then pharmacological TRPV4 activation should reproduce these defects in another vertebrate. Because *TRPV4* transcripts are detected in neural crest–derived jaw structures of zebrafish during early head development (*29*), we targeted TRPV4 activation in developing zebrafish larvae. Although zebrafish single ventricle heart anatomy limits our ability to assess conotruncal alignment defects, it offers an excellent model of craniofacial development. First, we confirmed that GSK101 activates zebrafish TRPV4 transiently expressed in CHO cells (Fig. 5A). We next used 1.4*cola1:egfp* transgenic zebrafish larvae that express *egfp* gene under the *cola1* promoter to drive expression in jaw structures (*30*) to monitor craniofacial development in live fish over time. We analyzed for craniofacial defects in zebrafish larvae treated at 2 days postfertilization (dpf) with GSK101 or GSK1153218 (a structurally related compound that lacks TRPV4 activity; table S1). By 3 and 4 dpf, only GSK101-exposed larvae exhibited a significant reduction in jaw length, as indicated by the decreased distance between Meckel's and ceratohyal cartilages (Fig. 5, B to D). Moreover, histological examination revealed disruption of the cellular organization in the ethmoid plate, suggesting defective palatogenesis (fig. S10, A and B). Consistent with the developmental timing and observed phenotypes of our chick studies, these data demonstrate that the impact of aberrant TRPV channel activation on neural crest–derived craniofacial development extends beyond an avian model.

Remote activation of TRP channels in neural crest cells phenocopied fever-associated birth defects

To test the hypothesis that congenital defects can be caused by transient activation of TRPV channels specifically within neural crest cells, we needed temporal and cell-specific control over these channels during development. Under specific conditions, modified ferritin-bound TRPV channels can be remotely controlled in vivo using RF electromagnetic fields (*31–33*) or static magnetic fields (*34*). We engineered FeRIC (Fe^{3+} redistribution to ion channels) modifications to TRPV1 and TRPV4 channels to direct endogenous intracellular ferritin to the cytoplasmic domains of TRPV1 or TRPV4 channels. Specifically, we fused the ferritin-binding domain 5 (D5) of kininogen-1 (*35*) with the C-terminal cytoplasmic domain of either TRPV1 (TRPV1[FeRIC])

Fig. 2. Temperature-activated TRPV channels in avian and mammalian neural crest cells. (**A**) Images of chick primary explanted neural tubes (NT) expressing GCaMP6 after 24 hours in culture. The dashed box region shows migrating neural crest cells used in subsequent analyses (green arrowheads). (**B**) Change in GCaMP6 fluorescence in chick neural crest cells after exposure to 1 μM GSK101 (blue) or 1 μM GSK101 combined with 10 μM RN1734 (gray line). (**C**) GCaMP6 fluorescence in chick neural crest cells after exposure to 1 μM VaTx3 (arrow, blue line) or buffer alone (gray line). (**D**) Change in Fluo-4 fluorescence in mouse primary explanted neural crest cells from embryonic day 8.5 (E8.5) embryos in response to the indicated doses of GSK101. (**E**) Fluo-4 fluorescence in mouse primary explanted neural crest cells from E8.5 embryos in response to GSK101 (arrow, blue line) or to GSK101 and 10 μM RN1734 (gray line). (**F**) Changes in Fluo-4 fluorescence in mouse neural crest cells after exposure to 1 μM capsaicin (arrow, blue line) or to capsaicin and SB366791 (gray line). (**G**) Representative GCaMP6 fluorescence in chick primary neural crest cells after exposure to 40°C imaging buffer, followed by imaging buffer (pH 5). (**H**) Representative GCaMP6 fluorescence in chick primary neural crest cells after exposure to 40°C imaging buffer or GSK101 (blue) or in the presence of RN1734 inhibitor (gray line). (**I**) Averages of more than four separate experiments as in (H) analyzing the number of cells per condition, as indicated. Significance was determined using unpaired *t* test. *$P < 0.05$. The number of biological replicates is indicated by *n*, and/or the number of cells analyzed is indicated in the graphs in (B) to (F), (H), and (I).
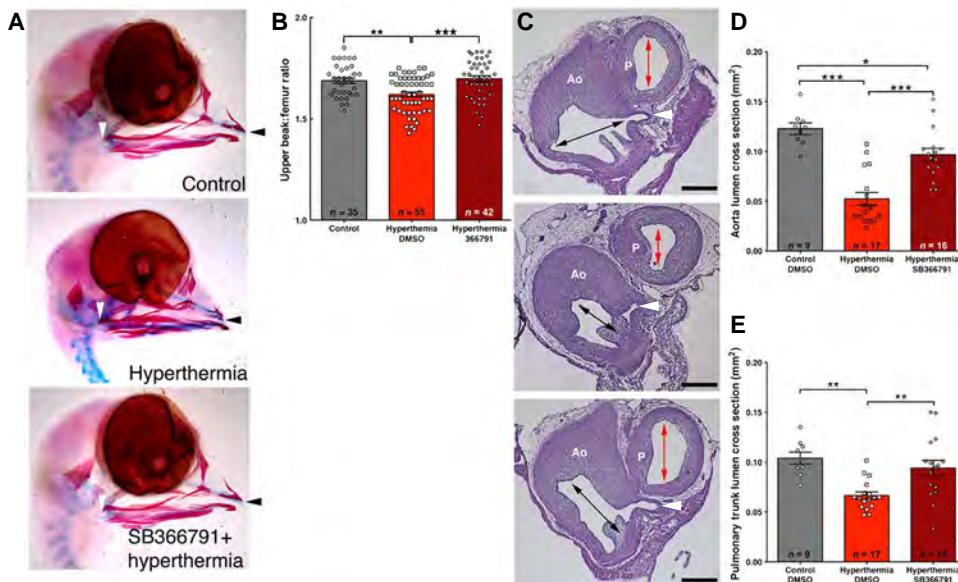
defects were detected in 20% of GSK101-exposed embryos at HH36 (Fig. 4, A and B, and fig. S9, A to D). GSK101 treatment also replicated the severe supravalvular stenosis, as indicated by a 50 and 44% reduction in luminal cross-sectional areas of the aorta and pulmonary trunk, respectively (Fig. 4, C to E). As in the hyperthermia-exposed chicks, GSK101-treated embryos had significantly shorter beak-to-femur ratios compared to controls (Fig. 4, F to H). Together, these data provide evidence that activation of TRPV4 channel permeability during critical windows of susceptibility can produce cardiac and craniofacial lesions that resemble those associated with maternal fevers in humans.

Fig. 3. TRPV1 inhibition rescues hyperthermia-induced congenital defects. (**A**) Alcian blue and alizarin red stains of HH36 heads from hyperthermia-exposed and hyperthermia-exposed chicks after pretreatment with the TRPV1 inhibitor SB366791. Upper beak measurement extended from the quadratojugal (white arrowhead) to the tip of the upper beak (black arrowhead). (**B**) Comparison of upper beak length–to–femur length ratios in control, hyperthermia, or hyperthermia + SB366791 chicks. (**C**) Histological sections through the aorta (Ao) and the pulmonary trunk (P) comparing the luminal areas (arrows) of control hearts (top), hyperthermia-exposed hearts (middle), and hyperthermia-exposed hearts with SB366791 pretreatment (lower) distal to the semilunar valves at the level of the left coronary artery (white arrowhead). Scale bars, 200 μm. (**D** and **E**) Cavalieri probe estimates of the luminal cross-sectional area of the aorta (D) or the pulmonary trunk (E) immediately above the aortic valve. Significance was determined by one-way analysis of variance (ANOVA), followed by Bonferroni's multiple comparisons test. *$P < 0.05$, **$P < 0.004$, and ***$P < 0.0001$. The number of biological replicates is indicated by n in the graphs in (B), (D), and (E).

or TRPV4 (TRPV4^{FeRIC}) to confer responsiveness to RF (Fig. 6, A and B, and figs. S11, A to C, and S12, A to C). By targeting endogenous ferritin found in cells, we eliminated the need for potentially cell-toxic exogenous iron administration or coexpression of modified ferritin (*32*, *36*).

To confirm FeRIC-mediated ferritin redistribution to the cell membrane, we investigated the subcellular localization of a ferritin heavy-chain mCherry fusion (FTH1^{mCherry}) protein in TRPV1^{WT}- and TRPV1^{FeRIC}-expressing HEK293T cells. In TRPV1^{WT} cells, FTH1^{mCherry} showed a cytoplasmic distribution consistent with normal FTH1 expression. However, when FTH1^{mCherry} was cotransfected with TRPV1^{FeRIC}, FTH1^{mCherry} was redistributed to the cell membrane by 24 hours (Fig. 6C). In addition, both TRPV1^{FeRIC} and TRPV4^{FeRIC} constructs, but not TRPV1^{WT}, TRPV4^{WT}, or FLAG construct, coimmunoprecipitated FTH1 (Fig. 6D). Next, we tested the influence of FeRIC-mediated ferritin redistribution on the bioavailability of cellular iron metabolism by measuring changes in four well-characterized iron-responsive genes. Redistribution of cellular ferritin using TRPV1^{FeRIC} or TRPV4^{FeRIC} did not significantly change mRNA concentrations of *Fpn1* (which encodes ferroportin-1), *TfR1* (which encodes transferrin receptor 1), *SLC11A2* (which encodes divalent metal transporter 1), or mRNAs encoding heavy and light chains of ferritin (fig. S13, A to E), suggesting that iron bioavailability was not substantially altered.
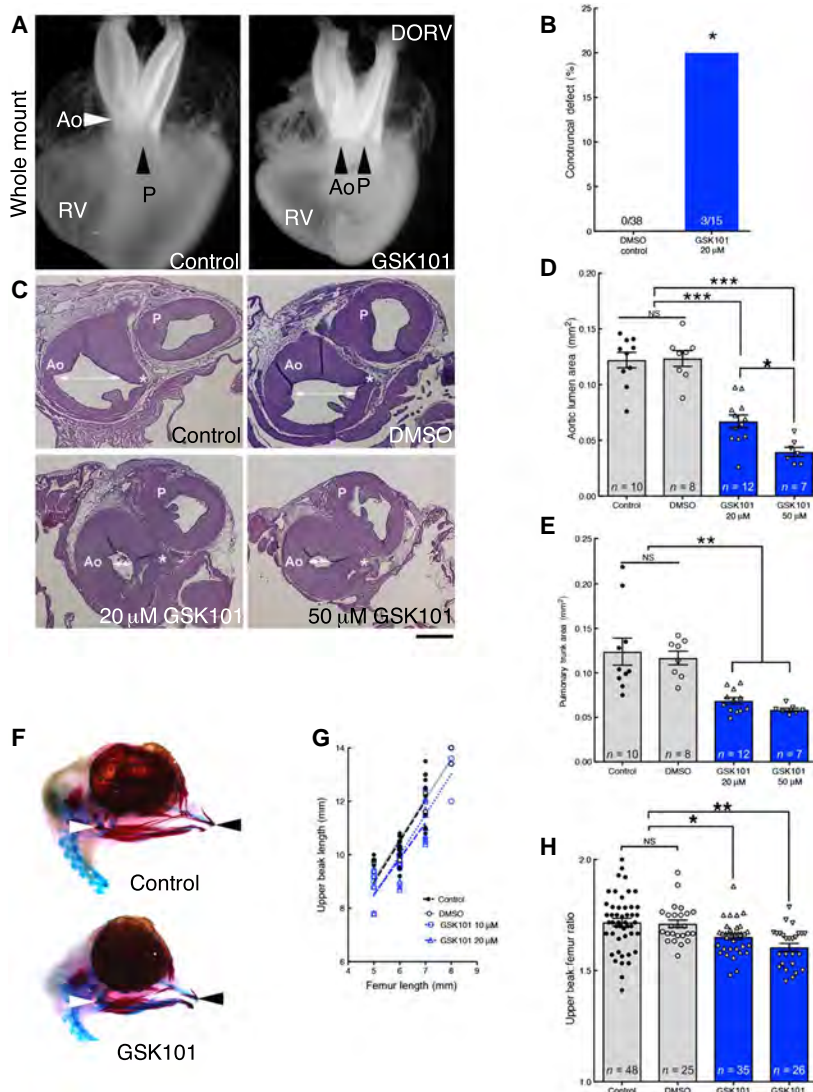
To remotely activate FeRIC channels, we used a 175-MHz RF coil that resonates at a frequency similar to that generated by a standard 3-T magnetic resonance imaging (MRI) scanner. The current in the RF coil was measured at 1.5 A peak to peak, generating a mean magnetic field of

36 μT and a specific absorption rate (SAR) of 6.8 W/kg (fig. S14, A to D). We confirmed that this magnetic field did not induce bulk temperature increases that could activate FeRIC channels by measuring the temperature of the cell media immediately before and after applying RF. The temperature fluctuation was measured at <±1°C. Because membrane-localized Fe^{3+} combined with RF could potentially be cytotoxic, we investigated cellular viability and membrane integrity. Treating TRPV1^{FeRIC}-positive HEK293T cells with 10 min of RF had no detectable impact on membrane integrity and did not affect cell viability at 24 hours (fig. S15, A to C). We next tested the responsiveness of TRPV1^{FeRIC} and TRPV4^{FeRIC} to RF in HEK293T cells coexpressing GCaMP6. RF stimulation of unmodified TRPV1^{WT} or TRPV4^{WT} did not alter Ca^{2+} permeability. However, channels responded to capsaicin (TRPV1; Fig. 6E) or GSK101 (TRPV4; Fig. 6F) agonists, as expected. Conversely, only TRPV1^{FeRIC} and TRPV4^{FeRIC} were transiently responsive to RF stimulation and their respective ligands. In both cases, the FeRIC-dependent RF responses were abolished in the presence of channel-specific inhibitors (Fig. 6, E and F). We next confirmed that remote activation of FeRIC channels required ferritin expression. Using clustered regularly interspaced short palindromic repeats (CRISPR)/CRISPR-associated protein 9 (Cas9), we deleted the ferritin heavy-chain gene (*FTH1*) in HEK293T cells (HEK$^{FTH1-KO}$; fig. S16, A to C). Deletion of *FTH1* abolished TRPV1^{FeRIC} responses to RF but did not interfere with capsaicin responses (fig. S16, D, E, and G). Transfection of HEK^{FTH1KO} cells with human *FTH1* rescued RF responsiveness to TRPV1^{FeRIC} (fig. S16, F and G).

To gain mechanistic insight into how RF activates TRPV1^{FeRIC}, we generated TRPV1$^{ΔT \, FeRIC}$, which has mutations that abolish temperature activation (N628K, N652T, and Y653T) (*37*) without affecting chemical sensitivity (fig. S17, A to C). When expressed in HEK293T cells, the FeRIC-modified triple mutant was not responsive to temperature changes, as expected, but retained its responsiveness to capsaicin (fig. S17, D and E). In addition to the disruption of temperature activation, these three point mutations also abolished RF-induced changes in permeability, suggesting that RF stimulation may act on TRPV1^{FeRIC} through a temperature-specific mechanism (fig. S17F).

We next sought to test whether cell-specific activation of the candidate TRPV channels phenocopied fever-associated heart defects. RF applied to chick neural crest cells expressing TRPV1^{FeRIC} increased Ca^{2+} permeability, which was blocked by the TRPV1 inhibitor SB366791 (Fig. 7A), thus confirming that TRPV1^{FeRIC} was responsive to RF in these cells. For in ovo experiments, TRPV1^{FeRIC} or TRPV1^{WT} plasmid DNA was bilaterally electroporated into premigratory neural crest cells at HH9. Expression of TRPV1^{FeRIC} alone did not appreciably affect neural crest cell migration to the pharyngeal arches at HH14 (Fig. 7B). Twenty-four hours after electroporation, eggs were either exposed for

Fig. 4. Ligand activation of TRPV4 replicates hyperthermia-induced birth defects. (**A**) Whole mounts of hearts from control and GSK101-treated embryos. The GSK101-treated heart showed DORV orientation of the aorta (Ao) and the pulmonary trunk (P). See fig. S9 for histological sections. Whole-mount and histological analysis of heart anatomy was performed in 38 hearts from DMSO-treated embryos and 15 GSK101-treated embryos. (**B**) Percentage of hearts with histologically confirmed conotruncal defects in GSK101-treated embryos compared to dimethyl sulfoxide (DMSO) controls. (**C**) Panel of histological sections through the aorta (Ao) and the pulmonary trunk (P) comparing the luminal areas (white arrows) at the level of the left coronary artery (*) in control, DMSO, and 20 or 50 μM GSK101 treatment. Scale bar, 200 μm. (**D** and **E**) Treatment with GSK101 reduced aortic luminal areas (D) [average coefficient of error (CE), 0.03] and pulmonary trunk luminal areas (E) (average CE, 0.03). (**F**) Alcian blue and alizarin red stains of DMSO control (top) and 20 μM GSK101-treated embryos (bottom) at HH36. (**G**) Normalization of upper beak length to femur lengths. (**H**) Graph of upper beak–to–femur ratios in untreated control, DMSO-treated control, and two GSK101 treatment groups. Significance was determined using Fisher's exact test (B) or one-way ANOVA, followed by Bonferroni's multiple comparisons test (D, E, and H). *$P < 0.03$, **$P < 0.004$, and ***$P < 0.0001$; NS, not significant. The number of biological replicates is indicated by n in the graphs in (D), (E), and (H).

only a single heart with an overriding aorta and VSD in RF[neg]TRPV1[FeRIC] embryos (Fig. 7D). Remotely induced conotruncal defects were rescued by pretreatment with the TRPV1 inhibitor SB366791 (Fig. 7D and fig. S18, A to L). To control for generalized RF effects, unelectroporated eggs were exposed to 10 min of RF and all unelectroporated RF[10min] control eggs had structurally normal hearts (Fig. 7D).

Next, we examined the vessels for outflow obstructive lesions and found no significant differences in cross-sectional luminal areas of the outflow tracts between TRPV1[WT] embryos with or without RF stimulation or between RF[neg]TRPV1[FeRIC] embryos and controls (Fig. 7, E to G). However, similar to hyperthermia and GSK101-exposed embryos, RF[10min]TRPV1[FeRIC] embryos displayed a 61 and 37% decrease in luminal cross-sectional areas in the aorta and pulmonary trunk, respectively (Fig. 7, E to G). Supravalvular stenosis was also rescued by pretreatment with SB366791 (Fig. 7, E to G).

We also analyzed the craniofacial structures in TRPV1[FeRIC]-expressing embryos after remote activation in cranial neural crest cells and compared them to RF[neg]TRPV1[FeRIC] controls. Remote activation of TRPV1[FeRIC] resulted in a significant reduction in upper beak length compared to control or RF[neg]TRPV1[FeRIC] embryos (fig. S19, A to C). These data demonstrate that transient activation of TRPV1 in cranial neural crest cells is sufficient to phenocopy craniofacial defects associated with maternal fevers.

We analyzed neural crest cell–specific remote activation of TRPV4[FeRIC] in chick neural crest explants. RF induced transient Ca^{2+} permeability in neural crest cells expressing TRPV4[FeRIC] that was blocked using RN1734 (Fig. 8A). Similar to FeRIC-modified TRPV1, remote activation of TRPV4[FeRIC] in neural crest cells produced a 57% incidence of conotruncal defects in the RF[10min]TRPV4[FeRIC] group compared to no defects in the RF[neg]TRPV4[FeRIC] group (Fig. 8, B and C). Remote activation of TRPV4[FeRIC] also resulted in significant supravalvular stenosis of the aorta and the pulmonary trunk (Fig. 8, B, D, and E). Together, these data indicate that transient activation of neural crest cell–specific TRPV1 or TRPV4 can replicate the types of clinically important heart defects that have been linked to maternal fevers in humans.

To confirm that FeRIC-mediated defects were not caused by RF-induced bulk temperature increases in tissues, we noninvasively

10 min to RF (RF[10min]) or not (RF[neg]). Of the TRPV1[WT] groups, RF[neg]TRPV1[WT] and RF[10min]TRPV1[WT] did not show conotruncal defects (Fig. 7, C and D). In contrast, RF[10min]TRPV1[FeRIC] embryos exhibited conotruncal alignment defects in 48% of the embryos (Fig. 7, C and D, and movie S1). These defects included overriding aorta, DORV, and tetralogy of Fallot and were accompanied by a perimembranous ventricular septal defect (VSD) (fig S18, A to L). In contrast, we observed
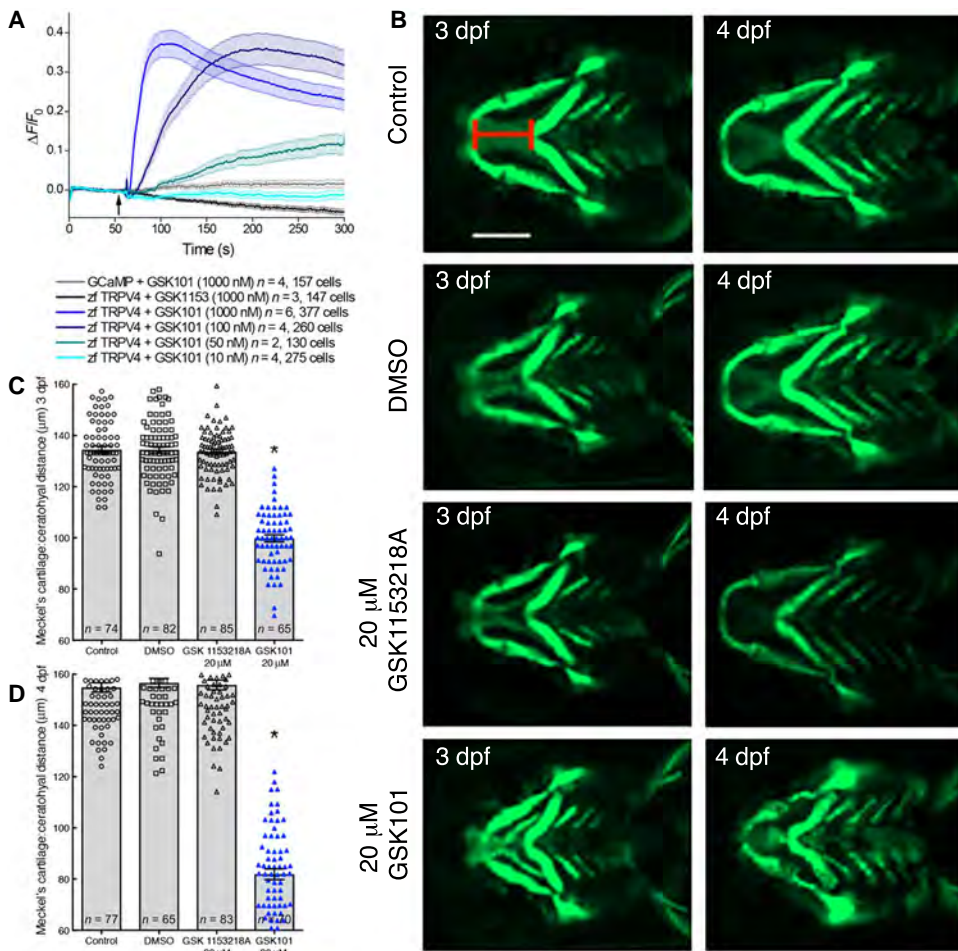
Fig. 5. TRPV4 activation disrupts jaw extension in zebrafish larvae. (**A**) Activity of GSK101 at the indicated concentrations and of GSK1153218 (black tracing), a structurally related compound that lacks activity on mammalian TRPV4 (table S1), in cloned zebrafish TRPV4 in CHO cells using GCaMP6 to assess Ca^{2+} permeability. (**B**) Representative images of *1.4cola1:egfp* transgenic zebrafish larvae treated with 20 μM GSK101, vehicle control, or GSK1153218A. Replicate batches were imaged live at 3 and 4 dpf. Scale bar, ~130 μm. (**C** and **D**) Quantification of the distance between Meckel's cartilage and the ceratohyal was measured [red line in (B)]. Significance was determined using one-way ANOVA, followed by Bonferroni's multiple comparisons test. *$P < 0.0001$ (GSK101-treated group compared to all other groups). The number of biological replicates is indicated by n, and/or the number of cells analyzed is indicated in the graphs in (A), (C), and (D).

those associated with human fever in the first trimester. We linked TRP channel activity to hyperthermia-induced defects by showing that TRPV1 inhibition during heat exposure mitigated most of the congenital defects. Both TRPV4 agonist and antagonists elicited similar neural crest cell–related defects under normothermic conditions. It is not uncommon for a gain or loss of function of a signaling pathway to result in similar defects, particularly in secondary heart field defects such as DORV. For example, in previous studies, we have shown that too much or too little FGF signaling in the pharynx (which is mediated by neural crest cells) results in proliferation of the secondary heart field progenitors or premature differentiation of the progenitors, respectively (17, 39, 40). Both result in a failure of the secondary heart cells to lengthen the outflow tract, which is necessary for proper outflow tract alignment. Similarly, Noonan and Leopard syndromes have overlapping cardiac and craniofacial phenotypes. Noonan syndrome is attributed to an activating mutation in *PTPN11* in 50% of patients, whereas Leopard syndrome is associated with an inactivating mutation in the same gene.

In our model, the timing of the hyperthermia and/or TRP channel activation in neural crest cells coincided with their migration into the pharyngeal arches. Whereas the immediate consequences of transient TRP channel activation in neural crest cells will be the focus of future studies, many studies have already shown that increased Ca^{2+} signaling affects cell migration, survival, and proliferation, all of which are linked to neural crest–associated heart and facial defects. Disruption of neural crest cell polarity is linked to conotruncal and craniofacial defects (41, 42). Increased maternal homocysteine is associated with neural crest–associated defects, and homocysteine enhances cardiac neural crest cell attachment and alters migration in vitro through a Ca^{2+}-dependent mechanism (43, 44). Further, increased Ca^{2+} homeostasis in neural crest cells is linked to human diseases including fetal alcohol syndrome and Timothy syndrome, both of which have neural crest–related craniofacial and/or conotruncal defects (45, 46). Together, these studies suggest that intracellular Ca^{2+} homeostasis is critical for normal neural crest–dependent development.

The study of environmentally induced transient alterations in genetically normal TRP channel activation has not been described in the context of congenital birth defects. In part, this may be due to the lack of widely available technology enabling precise temporal control of targeted cell-specific activation. Purely pharmacological approaches lack cell specificity and can be influenced by bioavailability through placental

mapped temperature changes throughout the egg and embryo at the beginning and end of the 10-min RF exposure using MRI thermometry (38). No substantial temperature differences were observed between RF^{10min} and RF^{neg} groups (fig. S20, A to H). Thus, RF exposure does not significantly heat the embryo to induce congenital defects, which is also supported by the 0% incidence of cardiovascular defects in control eggs exposed to RF (Fig. 7D).
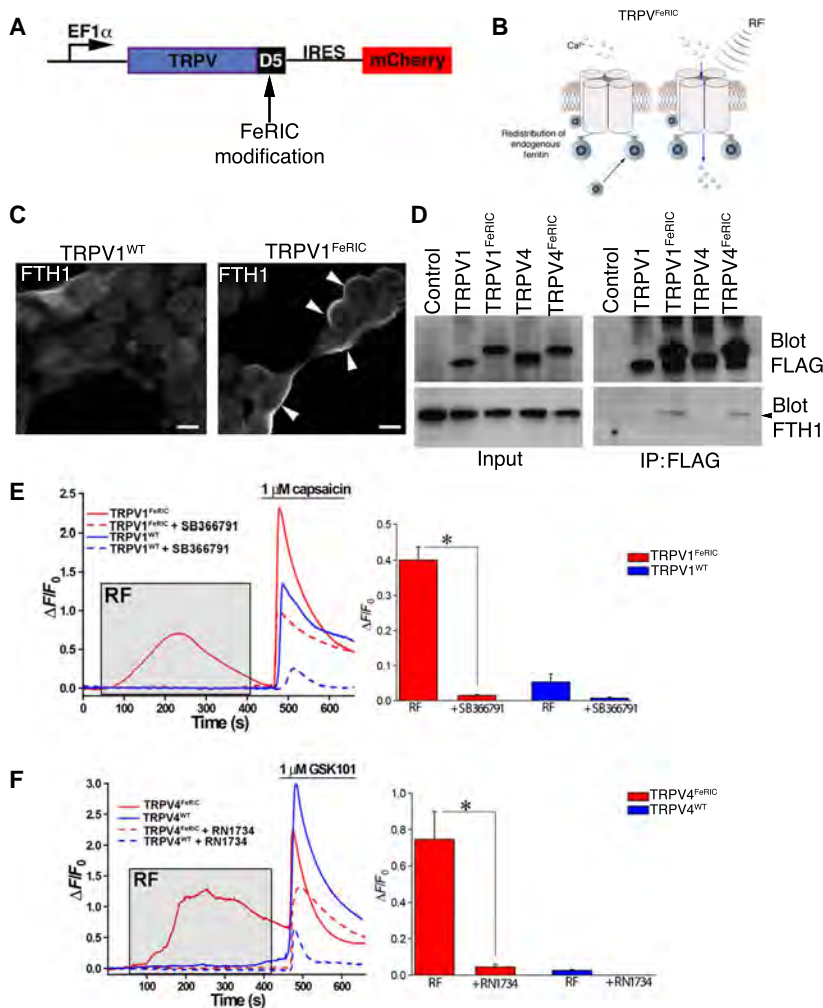
DISCUSSION
Our study identified the presence of two temperature-activated ion channels, TRPV1 and TRPV4, in cranial and cardiac neural crest cells during critical windows of heart and facial development. We demonstrated that experimentally controlled activation of these channels through temperature, pharmacological, or genetic approaches was sufficient to produce congenital heart and craniofacial defects similar to

Fig. 6. Development of remotely controlled TRPV^FeRIC channels. (**A**) TRPV channels were tagged with D5 of kininogen-1 and were cloned into the PLVX vector with an internal ribosomal entry site (IRES) for mCherry (figs. S12 and S13). (**B**) FeRIC channels were designed to recruit endogenous cellular ferritin to the modified TRPV channel at the cell membrane. (**C**) Cytoplasmic distribution of ferritin heavy chain fused with mCherry (FTH1^mCherry) in HEK293T cells expressing TRPV1^WT and membrane redistribution of FTH1^mCherry (white arrowheads) in TRPV1^FeRIC-expressing cells. Images were representative of two independent experiments. (**D**) Representative immunoprecipitation (IP) and Western blot of HEK293T cells expressing FLAG-tagged TRPV1^WT, TRPV1^FeRIC, TRPV4^WT, or TRPV4^FeRIC. The blot was probed for FLAG and FTH1. Four independent experiments were conducted using TRPV1^FeRIC, and three independent experiments were conducted using TRPV4^FeRIC. (**E**) GCaMP6 fluorescence in TRPV1^WT-expressing (blue) or TRPV1^FeRIC-expressing (red) HEK293T cells after RF (gray box) and then 1 μM capsaicin (bar). Bar graphs are $\Delta F/F_0$ averages of four experiments with 50 to 100 cells per group analyzed. (**F**) GCaMP6 fluorescence in TRPV4^WT-expressing (blue) or TRPV4^FeRIC-expressing (red) HEK293T cells after RF (gray box) and then 1 μM GSK101 (bar). Bar graphs are $\Delta F/F_0$ averages of five experiments with 106 to 123 cells per group analyzed. Significance was determined using unpaired t test. *$P < 0.05$.
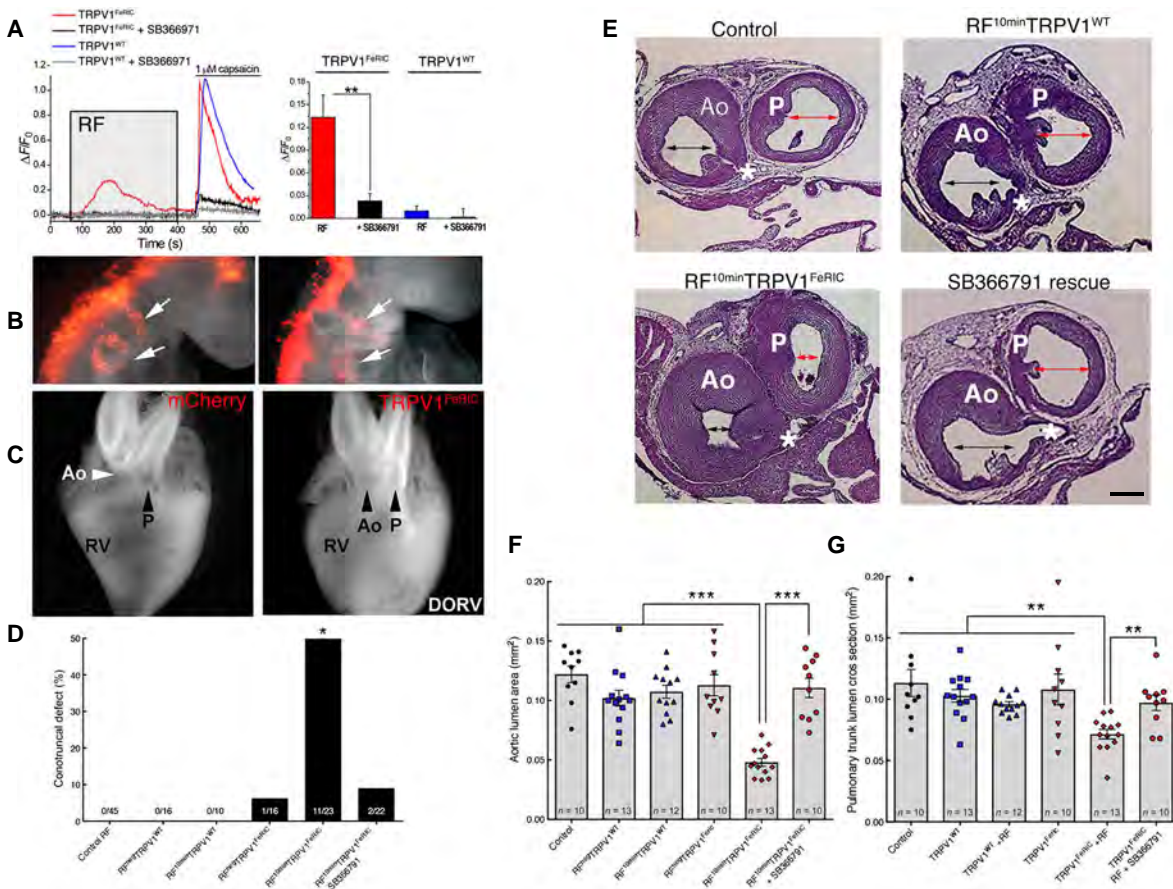
remove the compounds, and therefore, their effects could last hours to days depending on metabolism within the chick embryo. Our approach using RF offered the ability to precisely control the presence or absence of channel stimulus remotely. Here, we developed a simplified technology, FeRIC, that used the cell's endogenous iron stores to convert the modified channel into a remotely controlled channel with high temporal resolution and cellular specificity.

The physical mechanisms of ferritin-dependent electromagnetic control over ion channels are under debate (49, 50). The functionality of FeRIC channels is in line with functionalities of similar technologies independently developed by other laboratories (32, 34, 51). Here, we showed that FeRIC channels depended on the presence of endogenous intracellular ferritin. When the FTH1 gene was deleted in vitro, TRPV1^FeRIC was unresponsive to RF. Reintroduction of FTH1 in these cells rescued the remote capabilities of TRPV1^FeRIC. In another experiment, we showed that the introduction of temperature-sensitive amino acid substitutions in the outer pore region of TRPV1 also abolished RF-dependent channel activity. These data are suggestive but not conclusive evidence for a temperature-dependent mechanism. However, one important theoretical consideration suggests that RF waves at the power level reported in the literature are not sufficient to induce significant heating of ferritin (49). Thus, whether FeRIC-modified channels are activated by RF by a heat-dependent mechanism will require further measurements, such as nanoscale-resolution mapping of iron distribution and temperature change in unexposed and RF-exposed cells expressing these channels. Should this evidence become available, we anticipate that FeRIC modifications could be expanded to study other temperature-sensitive channels, both in the context of development and in relation to other spatiotemporally sensitive disease mechanisms.

Last, maternal infections with associated fevers in the first trimester are linked to clinically important craniofacial and cardiac defects. Craniofacial defects range from midface hypoplasia to clefts, and cardiac defects include obstructive lesions and conotruncal defects. Hyperthermia has been proposed as a direct teratogen; however, the mechanisms linking temperature to birth defects are unknown (52, 53). It is critical to distinguish between infection-based teratogenicity and simple hyperthermia because the latter is a modifiable risk factor. Acetaminophen is a drug commonly used by pregnant women and is safe and
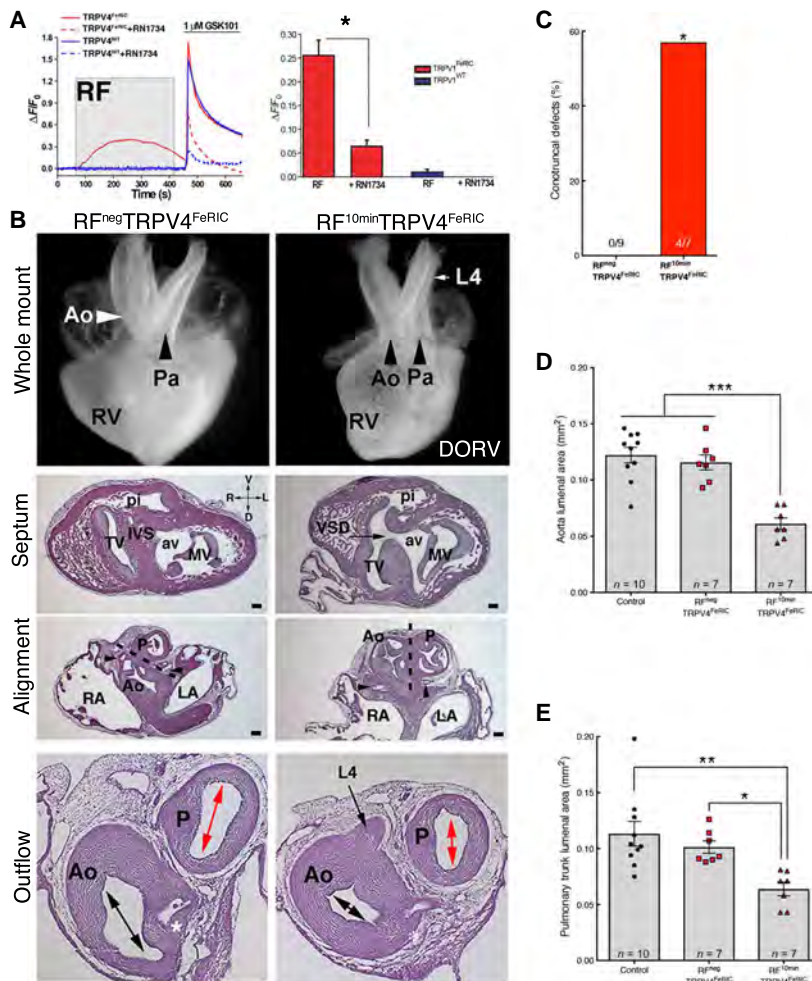
interfaces and maternal or fetal metabolism. Genetically modified channels with constitutive activity, or those that lack activity, can be targeted to cell-specific populations but cannot facilitate transient changes needed to study the impact of passing environmental factors such as fever. Technologies using synthetic designer ligands, such as DREADD (designer receptors exclusively activated by designer drug) receptor approaches, can provide cell specificity and some temporal resolution (47, 48). However, in our study, we needed much shorter restrictions on activation times to mimic the temperature spikes such as those that occur in febrile states. Once synthetic compounds used to activate DREADD receptors are injected into the egg, we would not be able to

Fig. 7. Fever-associated heart defects after remote activation of TRPV1 in neural crest cells. (**A**) GCaMP6 fluorescence in primary chick neural crest cells electroporated with TRPV1^{WT} (blue lines) or TRPV1^{FeRIC} (red lines) in the absence or presence of the TRPV1 inhibitor SB366971 (gray and black lines) after RF (gray box) and then 1 μM capsaicin (bar). Bar graph shows cumulative responses representing three to four separate experiments with 22 to 138 cells per group analyzed. (**B**) mCherry$^+$ neural crest streams migrating to the pharyngeal arches (white arrows) in HH14 control or TRPV1^{FeRIC} electroporated embryos. Images are representative of six independent experiments. (**C**) Whole-mount hearts from RF^{Neg}TRPV1^{FeRIC} embryo and RF^{10min}TRPV1^{FeRIC} embryo with arrows noting the position of the aorta (Ao) and the pulmonary trunk (P) with respect to the right ventricle (RV). Five independent experiments were performed. See movie S1 for an MRI reconstruction of an RF^{10min}TRPV1^{FeRIC}-induced DORV heart defect in chick. (**D**) Percentage of embryos with histologically confirmed conotruncal heart defects within indicated groups at HH36. (**E**) Representative histological sections through the aorta and the pulmonary trunk at the level of the coronary artery (*) in control RF, RF^{10min}TRPV1^{WT}, RF^{10min}TRPV1^{FeRIC}, and RF^{10min}TRPV^{FeRIC} with SB366791 pretreatment. The double arrowheads highlight the luminal areas of the aorta and the pulmonary trunk estimated using the Cavalieri probe. Scale bar, 200 μm. (**F**) Graph of the Cavalieri probe estimates of cross-sectional areas through the aorta at the level of the coronary artery in the indicated treatment groups (CE, 0.03). (**G**) Graph of the Cavalieri probe estimates of the cross-sectional areas through the pulmonary trunk distal to the semilunar valve in the indicated treatment groups (CE, 0.03). Significance was determined using unpaired *t* test (A), Fisher's exact test (D), or one-way ANOVA, followed by Bonferroni's multiple comparisons test (F and G). *$P < 0.02$, **$P < 0.005$, and ***$P < 0.0001$. The number of biological replicates is indicated by *n* in the graphs in (F) and (G).

protects against some fever-associated birth defects (*8*, *54*, *55*). However, new concerns have been raised over its repetitive use in pregnancy and the risk for behavioral problems in childhood (*56*). Our data provide a rational molecular mechanism for hyperthermia-induced teratogenicity mediated through transient gating of temperature-activated ion channels in neural crest cells. Because hyperthermia is a modifiable risk factor in pregnant women, these fever-associated birth defects may be preventable through public awareness and judicious use of antipyretics in febrile pregnant women. We hope that these observations will stimulate detailed clinical studies with a view to implement new policies in prenatal care and allow pregnant women to fully weigh the risks and benefits of antipyretic therapy during pregnancy.

MATERIALS AND METHODS
Animals
All animal experiments were approved by the Duke University Animal Care and Use Committee and were performed in accordance with the institutional and National Institutes of Health ethical guidelines. Fertilized Ross Hubert chick eggs (*Gallus gallus domesticus*, Mountaire Farms) were incubated for 1 to 10 days at 37°C and 70% humidity. Embryos were staged according to Hamburger and Hamilton (*57*). Adult zebrafish (*Danio rerio*) and the Tg-*1.4col1a1:egfp* line were maintained at 28°C on a 14-hour light/10-hour dark cycle. Embryos were raised at 28°C and staged according to days postfertilization and morphology. Embryos were grown in E3 medium (5 mM NaCl, 0.17 mM KCl, 0.33 mM CaCl$_2$, 0.33 mM MgSO$_4$,

Fig. 8. Fever-associated heart defects after remote activation of TRPV4 in neural crest cells. (**A**) GCaMP6 fluorescence in chick neural crest cells electroporated with TRPV4^{WT} (blue lines) and TRPV4^{FeRIC} (red lines) after RF (gray box) and then GSK101 (bar). TRPV4 inhibitor RN1734 inhibits response (dashed lines). Bar graph shows cumulative responses representing four separate experiments with 45 to 49 cells per group analyzed. (**B**) Whole-mount and histological sections of HH63 hearts from RF^{Neg}TRPV4^{FeRIC} embryo and RF^{10min}TRPV4^{FeRIC} embryo with DORV and a persistent L4 arch artery. The white and black arrowheads in the whole-mount images highlight the alignment of the aorta (Ao) and the pulmonary trunk (P) in the RF^{Neg}TRPV4^{FeRIC} and RF^{10min}TRPV4^{FeRIC} hearts. Histological sections of the whole mount in RF^{neg}TRPV4^{FeRIC} and RF^{10min}TRPV4^{FeRIC} hearts (above) at the level of the ventricular septum (IVS), at the level of the semilunar valves of the aorta (coronary arteries; black arrowheads) and the pulmonary trunk, and more distally through the smooth muscle walls of the aorta and the pulmonary trunk at the level of the left coronary artery (*). The dashed line indicates the plane of outflow tract septation. Black arrows indicate a VSD and persistent L4 arch artery in the section through the RF^{10min}TRPV4^{FeRIC} heart. Double-headed arrows indicate the luminal cross-sectional areas of the aorta and the pulmonary trunk measured in the Cavalieri estimates in (D) and (E). Scale bars, 200 μm. Three separate experiments were performed, and a total of nine RF^{Neg}TRPV4^{FeRIC} and seven RF^{10min}TRPV4^{FeRIC} hearts were analyzed. av, aortic vestibule; pi, pulmonary infundibulum; RA, right atrium; LA, left atrium. (**C**) Percentage of histologically confirmed conotruncal defects in RF^{Neg}TRPV4^{FeRIC} embryos compared to RF^{10min}TRPV4^{FeRIC} embryos. (**D**) Graph of the Cavalieri probe estimates of cross-sectional areas through the aorta at the level of the coronary artery in the indicated treatment groups (CE, 0.05). (**E**) Graph of the Cavalieri probe estimates of the cross-sectional areas through the pulmonary trunk distal to the semilunar valve in the indicated treatment groups (CE, 0.05). Significance was determined using unpaired *t* test (A), Fisher's exact test (C), or one-way ANOVA, followed by Bonferroni's multiple comparisons test (D and E). *$P < 0.02$, **$P < 0.005$, and ***$P < 0.0001$. The number of biological replicates is indicated by *n* in the graphs in (C) to (E).

Cell lines

Where indicated, the HEK cell line (HEK293T; cat. #632180, Clontech) or CHO cell line [ATCC (American Type Culture Collection) CCL-61] was used. Both cell lines have tested negative for *Mycoplasma* contamination by Clontech or ATCC, respectively. The identity of HEK293T cell line was verified by short tandem repeat analysis at Clontech. The identity of CHO cell lines was confirmed at the ATCC using an isoenzyme (interspecies) assay for hamster.

Hyperthermia experiments

Chick embryos were incubated at 37°C until the desired age (HH9 to HH15). The eggs were then placed in an incubator at 40° to 42°C. Internal egg temperature was monitored every 15 min using a digital thermometer probe. It generally took 45 to 60 min for the eggs to reach the targeted temperature. Once the target temperature was achieved, the eggs were incubated for another 60 min. After hyperthermia, embryos were reincubated at 37°C and allowed to develop until day 10 (HH36). The embryos were harvested, and gross congenital defects were documented. All hearts and heads were further processed and analyzed for structural defects (see below). Hyperthermic exposures of 40° to 41°C at HH11 to HH13 produced the most consistent defects. For the hyperthermia rescue experiments, embryos were pretreated with either 10 μM SB366791 or 0.1% DMSO in phosphate-buffered saline (PBS), incubated at 41°C for 1 hour, as described above (see below for details on drug delivery), returned to a 37°C incubator, and harvested at HH36 for analysis of heart and craniofacial defects.

Pharmacological treatments of chick embryos

Eggs were windowed at HH11 to HH14 and treated with 20 μl of varying concentrations of TRPV channel agonists or antagonists (see below) to determine the effective dose range. Controls included untreated embryos and DMSO-vehicle controls. The eggs were sealed with tape, incubated until HH36, and analyzed for heart and craniofacial defects. All drug stocks were made in DMSO. Stocks were

and 0.00001% methylene blue). All embryos (chick or zebrafish) were stage-matched and randomized to the specific treatment groups described below. The investigator was not blinded to the various treatment groups.

diluted in PBS such that the DMSO concentration was never higher than 0.1% and all treatments were delivered to the embryo at a volume of 20 μl. We determined the effective GSK101 (TRPV4 agonist) dose to be 20 μl of a 10 to 50 μM solution per egg (final concentration of ~3.3 to

16.7 nM in an average egg volume of 60 ml). The incidence and severity of defects increased at the higher doses. Lower doses did not induce defects, and no concentration tested caused lethality. Eggs dosed with the 10 to 100 μM RN1734 (final concentration of 1.2 to 12 nM) caused significant incidence of heart and craniofacial defects. For the hyperthermia and TRPV1^{FeRIC} rescue experiments, embryos were treated with 10 μM SB366791 (final concentration of 1.0 nM).

TRPV RT-PCR
Total RNA was extracted from HH14, HH22, or dissected HH9 neural folds. Complementary DNA (cDNA) was used in subsequent PCR reactions using the following published primer sets: GTCCTGCATA-GACACATGT [chick *TRPV1*(F)] and GCACAAAATACTGTATCCC [chick *TRPV1*(R)] (*58*); CCCTTGGAGTCACCTTACC [chick *TRPV2*(F)] and CTTCCCAGTCTTTGCATCT [chick *TRPV2*(R)] (*59*); CCCCTCAATTCACTCCTGC [chick *TRPV3*(F)] and GGAAAGGCA-TTCACCACCA [chick *TRPV3*(R)] (*59*); TTCAAGGATTGGGCATACG [chick *TRPV4*(F)] and ATTAACCCTCACTAAAGGG-CAACTTCCAGATGTGTTTG [chick *TRPV4*(R)] (*58*); GCCTG-CCTTCAAAATGCCACGCTCCTTCCTGG [chick *SLUG*(F)] and GGCTGCTGCGTAGCACACTGAGTCATGCAGTC [chick *SLUG*(R)] (*60*).

For the flow-sorted chick neural crest explant studies, a plasmid encoding GFP was electroporated at HH9 into the neural tube. The electroporated embryos were removed, and the neural tubes were enzymatically dissociated from the surrounding tissue. Specifically, the cranial and cardiac neural crest region extending from the midbrain to the third somite was placed in a solution containing dispase (0.5 μg/ml) and collagenase (1 μg/ml) for 1 to 2 min. The embryos were then placed in a stop/wash solution of Dulbecco's modified Eagle's medium (DMEM) with 20% fetal bovine serum (FBS), and the surrounding tissues were dissected away from the neural tube using fine needles. The isolated neural tubes were cultured on fibronectin-coated plates overnight at 37°C in DMEM with 20% FBS supplemented with 2% chick embryo extract. Twenty-four hours after plating, the neural tubes were mechanically removed with fine forceps. The remaining neural crest cells were treated with 0.25% trypsin for 2 min at 37°C, collected, and washed in DMEM with 20% FBS. The cells were sorted in the Duke Flow Cytometry Core Facility on a MoFlo XDP (Beckman Coulter Life Sciences).

In situ hybridization and immunohistochemistry
Whole-mount in situ hybridization was carried out using a standard protocol with digoxigenin (DIG)–labeled probes (*61*). Previously published probes were used for *TRPV1* and *TRPV4* in situ hybridizations (*58*). PCR-amplified probe templates were cloned and sequenced at the Duke Cancer Biology Sequencing Facility. Plasmids containing probe sequences were used to generate RNA probes from the T7 or SP6 promoters in vitro. After visualization of DIG, the embryos were embedded in paraffin, sectioned, and photographed to document the cellular localization of *TRPV1* and *TRPV4* transcripts. To determine colocalization of *TRPV1* and *TRPV4* transcripts with neural crest cells, the slides were soaked in PBS to remove the coverslips from the sectioned in situ hybridizations. Tissue sections were stained with mouse immunoglobulin M HNK1 antibody (ATCC) overnight at 4°C and developed with 3,3′-diaminobenzidine tetrahydrochloride. All images were acquired on a Leica DMRA2 compound microscope.

Plasmids
To generate the TRPV1^{WT} construct, full-length murine wild-type TRPV1 was PCR-amplified from cDNA generated from spinal cord

tissue from C57BL6 mice. 5′ Spe I sites and 3′ Not I sites were introduced into their respective locations outside the open reading frame using PCR. This product was subcloned into Spe I and Not I sites within the multiple cloning site of the PLVX-IRES-mCherry vector to generate TRPV1^{WT} (Clontech; for a detailed map, see fig. S12). To generate the TRPV1^{FeRIC} construct, PCR primers were designed to eliminate the 3′ stop site in wild-type TRPV1 and introduce a novel 3′ Xba I site. PCR primers introducing a 5′ Xba I site and a 3′ Not I site and a stop codon were used to amplify human kininogen-1 D5 (FeRIC) from whole-blood DNA. This FeRIC fragment was subcloned into the Xba I and Not I sites within the PLVX-IRES-mCherry vector (for a detailed map, see fig. S12). All completed constructs were sequence-verified by the Duke Cancer Biology Sequencing Facility and analyzed using MacVector 13.0.

To generate the TRPV1$^{\Delta T\ FeRIC}$ construct, a synthesized cassette of a 798–base pair (bp) region was designed, which included a native TRPV1 PsHA I restriction site, introduced the code for triple mutant amino acids N628K, N652T, and Y653T, and removed the native stop codon. We added a novel Xba I restriction site for ligation in-frame with the FeRIC sequence. Synthesis of the cassette was carried out by Bio Basic Inc. Original TRPV1^{FeRIC} construct was digested by PsHA I and Xba I, which removed the 3′-terminal end of TRPV1 ending at the FeRIC start. The PsHA I–Xba I mutant cassette was then ligated into the corresponding sites in the TRPV1^{FeRIC} construct. Complete construct with these three mutations was sequence-verified by the Duke Cancer Biology Sequencing Facility and analyzed using MacVector 13.0.

To generate the TRPV4^{WT} construct, we used full-length rat *TRPV4* cDNA, which was a gift from R. Lefkowitz (Duke University). Spe I and Not I restriction sites were introduced using PCR, as described above. The full-length wild-type *TRPV4* was subcloned into the PLVX-IRES-mCherry vector to generate TRPV4^{WT} (Clontech; for a detailed map, see fig. S13). To generate the TRPV4^{FeRIC} construct, PCR primers were designed to eliminate the 3′ stop site in wild-type *TRPV4* and introduce a 3′ Not I site. PCR primers introducing a 5′ Not I site and a 3′ Bam HI site and a stop codon were used to amplify human *Kininogen1 domain 5* (FeRIC). This FeRIC fragment was subcloned into the Xba I and BamH 1 sites within the PLVX-IRES-mCherry vector containing *TRPV4* (for a detailed map, see fig. S13). All completed constructs were sequence-verified by the Duke Cancer Biology Sequencing Facility and analyzed using MacVector 13.0.

Full-length chick *TRPV4* was synthesized and sequence-verified by Bio Basic Inc. The full-length construct was subcloned into the PLVX expression vector using novel Spe I (5′) and Not I (3′) sites introduced outside the open reading frame. Full-length zebrafish *TRPV4* was cloned from pooled zebrafish larval cDNA generated from embryos at 24 to 96 hours postfertilization (hpf) using the following 5′ primer containing a novel Spe I site and the 3′ primer containing a novel Xba I site: CTATTTCCGGTGAATTCCTCGAGACTAGTCTGGC-CATGACAGAGTCCTTGTCTG [*zfTRPV4*(F)] and CGGGATCCGCGGCCGCTCTAGATTAGCTTTCAGACTT-GAGTCGG [*zfTRPV4*(R)]. All constructs were sequence-verified by the Duke Cancer Biology Sequencing Facility and analyzed using MacVector 13.0.

To generate the FTH1 constructs, the full-length human *FTH1* was cloned using RT-PCR and cDNA generated from FeCl$_2$-stimulated HEK293T cells. Primers 5′-GCCGCCATGACGACCGCGT-3′ and 5′-CCGAGGCTTAGCTTTCATT-3′ flank the entire open reading frame. The entire open reading frame was cloned into pcDNA 3.1. For the FTH1^{mCherry} fusion construct, PCR was used to abolish the *FTH1* stop codon and to subclone the resulting *FTH1* construct into the multiple

cloning site of the pLVX-mCherry-N1 vector (Clontech) in-frame with mCherry. Sequences were verified by the Duke Cancer Biology Sequencing Facility and analyzed using MacVector 13.0.

CRISPR/Cas9 FTH1 deletion

Ferritin heavy chain (*FTH1*) was deleted in HEK293T cells using commercially available double nickase plasmids (Santa Cruz Biotechnology Inc.). This system uses two 20-nucleotide guide RNA (gRNA) sequences targeting exon 2 of the human *FTH1* gene. Briefly, cells were transfected with plasmids encoding the gRNA sequences, Cas9, and the puromycin resistance gene. Twenty-four hours later, transfected cells were selected in DMEM containing puromycin (5 mg/ml) for 5 days. Surviving cells were harvested, washed, and serially diluted into a 96-well plate. Wells containing single cells were expanded and screened by RT-PCR for full-length *FTH1* mRNA using the primers listed above. Full-length *FTH1* PCR products were cloned, and the expected 147-bp sequence deletion was confirmed in exon 2 of *FTH1*. Eighty-eight percent of the individual clones generated were FTH1-negative by RT-PCR and Western blot. HEK^{FTH1KO} clone 2 was expanded and used for subsequent TRPV1^{FeRIC} RF analysis in this study.

RF coil

The RF emitting coil consisted of a double loop wire with a loop diameter of about 4 cm. The coil was connected in parallel with tuning capacitors forming an LC circuit. The circuit was tuned to a resonance frequency at about 175 MHz. RF signal was generated by a broadband (0 to 400 MHz) signal generator (model 102A, Boonton Electronics) and amplified using a 50-W linear RF amplifier (model 550L, Electronic Navigation Industries). Electric current across the coil was measured using a current monitor (model 2877, Pearson Electronics). The peak-to-peak current was measured to be 1.5 A. During experiments, the coil sits roughly 1.5 cm above the cells or chick embryo.

RF simulation

The electromagnetic fields emitted by the RF coil were computed by cylindrical finite-difference time-domain simulation in MATLAB (version R2014a, Mathworks), as described by Dib and Weller (*62*). Perfectly matched layer boundary conditions were implemented as described by Berenger (*63*), and the simulation resolution was 0.5 cm in the *z* direction, 0.25 cm in the radial direction, and $\pi/28$ radians in the ϕ direction. The computed magnetic field was verified by comparison with the analytical expression for the magnetic field along the axis of a static current loop. The electromagnetic fields were simulated for a coil loaded with a dish of 0.5-cm thickness and 2-cm radius. The dish electrical conductivity was 0.5 S/m, similar to human tissue (*64*). The ac input was 1.5 A peak to peak at 175 MHz.

Bilateral electroporations and RF delivery to eggs

For the cranial and cardiac neural crest cell electroporation studies, eggs were incubated to HH9 to HH11. The eggs were windowed, and the vitelline membrane was torn. One or two drops of Ringer's solution were applied so that the embryo fell away from the vitelline membrane. Platinum electrodes were placed at the cranial end on either side of the embryo. TRPV1^{WT}, TRPV1^{FeRIC}, TRPV4^{WT}, or TRPV4^{FeRIC} constructs were injected into the neural tube using a glass micropipette. DNA concentration was 4 μg/μl. Four 50-ms square-wave pulses were immediately applied at 20 V each. A drop of Ringer's solution was again applied to the embryo, and injection and electroporation were repeated for the other side of the neural tube. Twenty-four hours after electroporation,

the expression of the plasmid was confirmed by visualizing mCherry expression. Then, the egg was placed in a 37°C chamber, the RF coil was placed on the egg surrounding the embryo, and 10 min of RF stimulation (see above) was delivered. Control (RF^{Neg}) eggs were placed in the same 37°C chamber for 10 min without RF stimulation. For the TRPV1^{FeRIC} rescue experiments, TRPV1^{FeRIC}-expressing embryos were pretreated with 10 μM SB366791 for 1 hour before RF exposure.

Primary neural crest cell cultures

A mixture of GCaMP6 (obtained from Addgene #40753) (*65*) was electroporated alone or in combination with the TRPV constructs described above into chick neural tubes at HH9. The electroporated embryos were removed from the egg, and the neural tubes were enzymatically dissociated from the surrounding tissue. Specifically, the cranial and cardiac neural crest region extending from the midbrain to the third somite was placed in a solution containing dispase (0.5 μg/ml) and collagenase (1 μg/ml) for 1 to 2 min. The embryos were then placed in a stop/wash solution of DMEM with 20% FBS, and the surrounding tissues were dissected away from the neural tube using fine needles. The isolated neural tubes were cultured on fibronectin-coated plates overnight at 37°C in DMEM with 20% FBS supplemented with 2% chick embryo extract, and Ca^{2+} imaging was performed as described below. Mouse neural crest cell explants were generated as above using E8.5 embryos from CD1 mice. Mouse neural tubes were cultured at 37°C in DMEM with 20% FBS.

Ca^{2+} imaging

HEK293T or CHO cells were plated on collagen-coated, glass-bottom 35-mm dishes and cultured in 10% FBS and 1% PenStrep in DMEM. After 24 hours, cells were cotransfected using the Lipofectamine LTX Plus reagent with GCaMP6 and either TRPV1^{WT}, TRPV1^{FeRIC}, TRPV4^{WT}, or TRPV4^{FeRIC}. For Ca^{2+} imaging of chick neural crest cells, neural crest cells were electroporated, isolated, and cultured as described above. Twenty-four hours after electroporation, cytosolic Ca^{2+} were monitored by fluorescence imaging of cells positive for GCaMP6$^+$ and TRPV channels (mCherry$^+$) using a 20× objective on an inverted Olympus IX50 microscope equipped with a camera (QImaging Retiga 1300i) controlled by Metamorph software 7.8 (Molecular Devices). Images were captured at 1 frame/s. Unless stated otherwise, all experiments were carried out at room temperature. Neural crest cell recordings were carried out in Leibovitz's L-15 medium (Thermo Fisher Scientific) supplemented with Ca^{2+} to a final concentration of 2 mM. For HEK293T cells, the imaging buffer solution contained 140 mM NaCl, 2.8 mM KCl, 1 mM MgCl$_2$, 2 mM CaCl$_2$, 10 mM glucose, and 10 mM Hepes at pH 7.4. RF was delivered for 10 min using a custom-built RF-emitting coil designed to fit the 35-mm tissue culture dish, as described above. After RF, cells were then exposed to TRP channel agonists, 1 μM capsaicin or 1 μM GSK101. In a second series of experiments, HEK293T or neural crest cells were exposed to TRPV1 or TRPV4 channel inhibitors (10 μM SB366791 or 10 μM RN1734) for 10 min and then imaged for changes in intracellular Ca^{2+} with or without RF exposure. Images were analyzed using Metamorph software; cytosolic regions of interest (ROIs) were placed over those cells that coexpressed GCaMP6 and TRPV channels. GCaMP6 fluorescence intensity was measured for each image of the time-lapse acquisition (650 s). The data were fit with a double exponential decay time and corrected for photobleaching using Microcal Origin 7 software (OriginLab). Responses are presented as $\Delta F/F_0$, where F_0 is the resting fluorescence averaged over 60 s before the start of stimulation and ΔF is the change in fluorescence over resting values. For each experimental condition, 50 to 150 cells

were analyzed, and each experiment was conducted at least three times. Plots in the individual figures are representative tracings.

To image Ca^{2+} changes in mouse neural crest cells, neural tubes from E8.5 embryos were dissected and plated as described above. Eight to 24 hours after culture, cells were washed with imaging buffer solution and incubated with 5 μM fluo-4 AM (Molecular Probes) for 40 min at room temperature. Fluo-4–loaded cells were imaged using the imaging system described above. Fluo-4 was excited using a blue filter, and green emission was collected at 1 frame/s. Functional TRPV1 channels were analyzed by exposing the explants to 1 μM capsaicin 8 to 18 hours after plating. SB366791 (10 μM) was used to block capsaicin-mediated Ca^{2+} responses. To assess TRPV4 channels, neural crest cell explants were exposed to GSK101 (0.1 to 1000 nM) after 8 to 24 hours in culture. The TRPV4 inhibitor RN1734 (10 μM) was used to inhibit the GSK101-mediated response. Data were analyzed off-line with MetaMorph Image Analysis software. Changes in cytosolic Ca^{2+} were estimated as the relative increase of fluorescence intensity (F) from baseline fluorescence (F_0).

Temperature activation Ca^{2+} imaging assays

Temperature sensitivity of TRPV channels was examined at a hyper-thermic (40°C) temperature in neural crest cells or HEK293T cells transfected with GCAMP6 and either TRPV1^{FeRIC} or TRPV1$^{\Delta TFeRIC}$, using Lipofectamine LTX Plus reagent. Twenty-four hours later, trans-fected cells were identified by the expression of both GCaMP6 and TRPV1 channels (mCherry$^+$). Primary GCaMP6$^+$ chick neural crest cells were also generated as described above to examine the thermosensitivity of endogenous TRPV channels. For Ca^{2+} imaging, neural crest cells or HEK293T cells were placed on a recording chamber in the stage of a Nikon Eclipse Ti-S inverted microscope. Cells were epi-illuminated using a blue filter and continuously perfused with the imaging buffer solution through a gravity-driven perfusion system (~2 ml/min). Drugs were applied using the same gravity system. The temperature was controlled with a CL-100 temperature controller (Warner Instruments) and a SC-20 dual in-line heater/cooler (Harvard Apparatus). During experiments, temperature was monitored with a thermistor (TA-29, Warner Instruments) within the recording chamber. Heat stimulus was delivered stepwise to increase the temperature from 25° to 40°C over a 3-min period. After the removal of the heat stimulus, cells were exposed to TRPV channel agonists such as pH 5 or 1 μM GSK101. Neural crest cells were exposed to TRPV4 channel inhibitor 10 μM RN1734 for 10 min and then imaged for changes in intracellular Ca^{2+} with heat or GSK101 exposure. GCaMP6 green emission was collected from cells at 1 frame/s. Images were analyzed off-line using Nikon Element software; ROIs were placed over those cells that coexpressed GCaMP6 and TRPV channels or over the GCAMP6-positive neural crest cells for endogenous TRPV channel analysis. GCaMP6 fluorescence intensity was measured for each image of the time-lapse acquisition. Data were analyzed using Microcal Origin 7 software (OriginLab). Responses are presented as $\Delta F/F_0$, and plots correspond to average ± SEM.

Membrane integrity and cell viability assays

Membrane integrity assays were conducted in HEK293T cells in vitro. Membrane integrity was assayed using the LIVE/DEAD Fixable Green Dead Cell Stain Kit (Life Technologies) following the manufacturer's instructions. In this assay, the green dye is excluded from cells with in-tact membranes. However, in cells with disrupted membranes, the dye accumulates in the cell and reacts with cytoplasmic proteins. Briefly, mCherry- or TRPv1^{FeRIC}-expressing HEK293T cells were exposed to either no RF, RF for 10 min, or 10 min at 55°C. After 5 min, cells were

stained with the manufacturer's green fluorescent amine reactive dye and then fixed with 1% paraformaldehyde. Cells were analyzed using a 488-nm line of an argon-ion laser, and green fluorescence was detected in the green channel of the flow cytometer (530/30 nm).

Cell viability was measured with the CellTiter 96 Non-Radioactive Cell Proliferation assay (MTT, Promega). HEK293T cells (40 to 50% confluent) transfected with TRPV1^{FeRIC} or mCherry were exposed to RF for 10 min and cultured at 37°C for 30 hours before performing the assay according to the manufacturer's instructions. RF-exposed cells from each group were compared to transfected cells without RF exposure.

Immunoprecipitation

N-terminally FLAG-tagged wild-type and FeRIC-modified TRPV1 and TRPV4 were generated by PCR. HEK293T cells in a six-well plate were transfected with 3 μg of plasmid DNA using Lipofectamine PLUS re-agent (Invitrogen). Eight hours after transfection, culture medium was exchanged with fresh medium containing 100 μM $FeCl_2$ for endoge-nous ferritin induction. Eighteen hours later, protein was extracted and immunoprecipitation experiments were performed as described (66) with the following modification: CHAPS lysis buffer contained 5 mM CHAPS, 50 mM tris (pH 7.4), 150 mM NaCl, 1 mM CaCl, 5% sucrose, 0.5% Triton X-100, and protease inhibitor cocktail (Roche). Anti-FLAG M2 affinity gel (A2220, Sigma-Aldrich) was used to immuno-precipitate FLAG-tagged TRPV1 or TRPV4 constructs following the manufacturer's instructions. Samples were probed by Western blot using antibodies against DDDDK (1:2000; ab1170, Abcam) or FTH1 (1:1000; #3998, Cell Signaling).

Heart analysis

Hearts from various treatment groups were harvested at day 10, photo-graphed, fixed overnight in 10% formalin, paraffin-embedded, serially sectioned, stained with hematoxylin and eosin, and assessed for defects, as previously described (40). Briefly, the hearts were scored as DORV if the aorta or the aortic portion of the outflow was not wedged between the tricuspid and mitral valve and shifted to the right in relation to the pulmonary trunk. All hearts categorized as DORV had a concomitant VSD. Hearts were classified as overriding aorta if the outflow VSD was positioned such that the aortic vestibule was in communication with the pulmonary infundibulum and the aorta was overriding the septal defect. In embryos with abnormal persistence of arch artery vessels, only vessels with patent lumens were scored. Outflow obstruction lesions were qual-itatively assessed compared to stage-matched controls. Quantitative measurements were carried out as described below (see Stereology). Hearts from embryos with ectopia cordis were excluded from analysis because the etiology of the alignment defects cannot be distinguished between the experimental treatment and the open chest wall.

Stereology

Hematoxylin and eosin staining was performed on serial 10-μm sections through the entire heart from the ventricular apex through the aortic arch, as previously described (40). The aortic and pulmonary valves were identified. For the aorta, we began with the last section containing the coronary artery, and moving superiorly, the lumens in three to four adjacent tissue sections were analyzed. For the pulmonary trunk, we identified the last section with pulmonary valve tissue attached to the vessel wall and analyzed three to four tissue sections above that. Analysis was conducted in bright field using the Cavalieri probe in Stereo Investigator 11 (MBF Biosciences) on a Zeiss Axio

Imager 2 microscope. Analysis parameters include the following: tissue cut thickness, 10 μm; analysis objective, 10×; probe grid size, 50 μm × 50 μm; grid orientation, randomized. The results are presented as the average luminal area in square millimeters for each vessel. The average CE (Gundersen $m = 1$) is a standard statistical value that is used extensively in stereological studies. CE is defined as the SEM of repeated estimates divided by the mean. An average CE was reported for each of the experiments within the individual figures and was less than 0.05.

MRI thermometry

MRI thermometry was used to measure internal heating in chicken eggs due to RF. This technique uses the temperature-dependent chemical shift of water to measure internal temperature changes during the time between two MRI scans of a stationary object (38). TRPV1[FeRIC] was electroporated into the neural tube of chick embryos at HH9. Twenty-four hours later, eggs were imaged using a 7.0-T small-bore animal MRI scanner controlled by Agilent software version vnmr4. A multi-echo gradient echo sequence was used to measure frequency maps. The sequence parameters were as follows: field of view, 7 cm × 7 cm; matrix 128 × 128; repetition time, 200 ms; first echo time (TE_1), 5 ms; second echo time (TE_2), 10 ms; flip angle, 10°; slice thickness, 2 mm. Each scan took 20 s and was repeated every 10 min for 140 min, alternating 10-min periods of RF and no RF. The first two echoes of each scan were used to create 14 maps that measured changes in temperature during periods of RF and 14 maps that measured temperature changes without RF.

Anatomical MRI and heart visualization

Before MRI, embryo specimens were immersion-fixed in 2.5 mM ProHance (Gadoteridol, Bracco Diagnostics Inc.) dissolved in 10% formalin. ProHance, a gadolinium contrast agent, was used to decrease T_1 (longitudinal relaxation time) and to improve SNR (67). Images were acquired on a 9.4-T system (400-MHz vertical-bore Oxford superconducting magnet). The system consists of an 89-mm vertical-bore magnet controlled by an Agilent VnmrJ 4.0 console (Agilent Technologies). The specimens were firmly secured in an acrylic specimen cartridge and immersed in Fomblin (Ausimont USA Inc.) to limit susceptibility artifacts at the tissue boundary. The cartridge was placed in a copper solenoid RF resonator (diameter, 14 mm; length, 21 mm). A set of three-dimensional multiecho gradient echo images was acquired (10 echoes; TE_1/spacing/TE_{10}, 3.9/7.6/71.9 ms) with a field of view of $22 \times 11 \times 11$ mm^3 and a matrix size of 768 × 384 × 384, resulting in an isotropic resolution of $28.6 \times 28.6 \times 28.6$ μm^3. Final images were produced using a weighted sum of the individual echo images (68, 69).

One specimen was rotated to a position such that all four chambers of the heart were visible on a cross section. This position served as a reference. The coronal plane of this reference space was orthogonal to the atrial septum. Images were registered to this space using rigid body transformation, correlation cost function, and sinc interpolation [FMRIB (Functional Magnetic Resonance Imaging of the Brain) Software Library (https://fsl.fmrib.ox.ac.uk/fsl/fslwiki)]. The heart wall, chambers, and vessels were segmented using a seeded region growing in Avizo software (Visualization Sciences Group). The individual chambers (right atrium, right ventricle, left atrium, and left ventricle) and vessels (pulmonary artery and aorta) were further segmented manually at the respective valves.

Quantitative PCR for cellular Fe²⁺ homeostasis

HEK293T cells were transfected with control mCherry, TRPV1[WT], TRPV1[FeRIC], TRPV4[WT], or TRPV4[FeRIC]. Seventy-two hours after transfection, total RNA was extracted and cDNA was prepared using the High-Capacity cDNA Reverse Transcription Kit (Applied Biosciences). Quantitative PCR was performed using SYBR green (iQ SYBR Green Supermix; Bio-Rad) on a Bio-Rad C1000 Touch thermal cycler. mRNA expression was calculated using the $\Delta\Delta C_t$ method and normalized to the relative expression of β-actin. mRNA levels for mCherry were adjusted to 1. Primers used have been previously published (70). Primer sequences are as follows: TTGCAGGAGTCATTGCTGCTA [F*pn*(F)] and TGGAGTTCTGCACACCATTGAT [F*pn*(R)]; CCAT-CAACCGCCAGATCAAC [F*th*(F)] and GCCACATCATCTCGGT-CAAA [F*th*(R)]; GGGCCTCCTACACCTACCTC [F*tl*(F)] and CTCCTGGGTTTTACCCCATT [F*tl*(R)]; TGTTTGATTG-CATTGGGTCTG [*Slc11a2+IRE*(F)] and CGCTCAGCAG-GACTTTCGAG [*Slc11a2+IRE*(R)]; TCAAGCCAGATCAGCATTCTC [*Tfr1 ex 2,3*(F)] and AGCCAGTTTCATCTCCACATG [*Tfr1 ex 2,3*(R)].

Avian craniofacial analysis

To visualize the development of the skeletal structures, day 10 to day 11 chicks from various treatment groups were fixed in 95% ethanol and processed for alcian blue and alizarin red staining, as described by Wassersug (71). Once cleared in glycerol, the length of the jaw structures (in millimeters) was measured using a dissecting microscope fitted with an ocular micrometer. The upper beak measurement extended from the quadratojugal to the tip of the upper beak. To ensure comparable staging across treatment groups, the upper beak length for each chick was normalized to individual femur lengths.

Zebrafish pharmacological treatment and imaging

We treated zebrafish larvae at 2 dpf to assess the impact of TRPV4 stimulation on cranial neural crest cell convergent and extension. Zebrafish embryos were generated by natural pairwise matings of -1.4col1a1:egfp transgenic adults (AB background) (30) Embryos were collected 30 min after spawning, stored at 28°C in embryo medium [NaCl (0.3 g/liter), CaSO₄ (75 mg/liter), NaHCO₃ (37.5 mg/liter), and 0.003% methylene blue], and distributed randomly into separate petri dishes (50 embryos per dish). At 2 dpf, embryos were treated with either 20 μM GSK101 in 0.1% DMSO, 0.1% DMSO (vehicle control), or 20 μM GSK1153218A, a compound that is structurally similar to GSK101 but lacks detectible activity (table S1). We obtained ventral images of cartilaginous craniofacial structures at 3 and 4 dpf using the VAST (Vertebrate Automated Screening Technology; software version 1.2.2.8.) platform (Union Biometrica), as described (72). Embryos were collected after imaging and returned to their petri dish with fresh experimental medium and stored at 28°C until the 4-dpf imaging time point. Craniofacial defects were quantified by measuring the distance between Meckel's cartilage and the ceratohyal using ImageJ. All experiments were repeated at least three times.

Statistical analysis

All experiments, unless otherwise noted, were repeated a minimum of three times. Differences in categorical data sets (percentage of animals with congenital defects) were analyzed using Fisher's exact testing. Differences in continuous data sets were analyzed using a one-way ANOVA, followed by Bonferroni post hoc test or unpaired t test, where appropriate. Data are means ± SEM, where applicable. $P < 0.05$ was considered a statistically significant difference.

SUPPLEMENTARY MATERIALS

www.sciencesignaling.org/cgi/content/full/10/500/eaal4055/DC1
Fig. S1. Hyperthermia causes severe craniofacial defects in chicks.

Fig. S2. Hyperthermia causes aortic arch patterning defects in chicks.

Fig. S3. TRPV channel mRNA expression in neural crest cells.

Fig. S4. *TRPV1* transcripts are detected in cranial and cardiac neural crest cells by in situ hybridization.

Fig. S5. *TRPV4* transcripts are detected in cranial and cardiac neural crest cells by in situ hybridization.

Fig. S6. Activation of cloned chick TRPV4 and chick TRPV1 with channel-specific ligands.

Fig. S7. Neural crest cell–related congenital defects in chicks upon TRPV4 inhibition.

Fig. S8. TRPV1 inhibition partially rescues hyperthermia-induced conotruncal defects.

Fig. S9. Pharmacological activation of TRPV4 induces fever-related heart defects.

Fig. S10. TRPV4 activation disrupts palatogenesis in zebrafish larvae.

Fig. S11. *TRPV1* maps.

Fig. S12. *TRPV4* maps.

Fig. S13. Expression of FeRIC-modified TRPV1 does not alter cellular Fe^{2+} homeostasis.

Fig. S14. RF coil and SAR estimation.

Fig. S15. Membrane integrity and cell viability are unchanged in TRPV1^{FeRIC}-expressing cells after RF stimulation.

Fig. S16. Remote activation of FeRIC is ferritin-dependent.

Fig. S17. A temperature-insensitive TRPV1 mutant does not respond to RF.

Fig. S18. Histological analysis of HH36 hearts confirms conotruncal defects after transient activation of TRPV1^{FeRIC} by RF.

Fig. S19. Fever-associated craniofacial defects after remote activation of TRPV1 in neural crest cells.

Fig. S20. RF does not cause bulk tissue temperature changes in ovo.

Table S1. Structural and functional comparison of GSK101 and GSK1153218 (GSK-dead).

Movie S1. MRI reconstruction of a TRPV1^{FeRIC}-induced DORV heart defect in chick.

References (73–79)

REFERENCES AND NOTES

1. J. I. E. Hoffman, S. Kaplan, The incidence of congenital heart disease. *J. Am. Coll. Cardiol.* **39**, 1890–1900 (2002).

2. S. E. Parker, C. T. Mai, M. A. Canfield, R. Rickard, Y. Wang, R. E. Meyer, P. Anderson, C. A. Mason, J. S. Collins, R. S. Kirby, A. Correa; National Birth Defects Prevention Network, Updated national birth prevalence estimates for selected birth defects in the United States, 2004–2006. *Birth Defects Res. A* **88**, 1008–1016 (2010).

3. L. D. Botto, A. Correa, Decreasing the burden of congenital heart anomalies: An epidemiologic evaluation of risk factors and survival. *Prog. Pediatr. Cardiol.* **18**, 111–121 (2003).

4. M. J. Dixon, M. L. Marazita, T. H. Beaty, J. C. Murray, Cleft lip and palate: Understanding genetic and environmental influences. *Nat. Rev. Genet.* **12**, 167–178 (2011).

5. J. W. Dreier, A.-M. N. Andersen, G. Berg-Beckhoff, Systematic review and meta-analyses: Fever in pregnancy and health impacts in the offspring. *Pediatrics* **133**, e674–e688 (2014).

6. M. Csáky-Szunyogh, A. Vereczkey, Z. Kósa, B. Gerencsér, A. E. Czeizel, Risk and protective factors in the origin of conotruncal defects of heart—A population-based case–control study. *Am. J. Med. Genet. A* **161A**, 2444–2452 (2013).

7. L. D. Botto, J. D. Panichello, M. L. Browne, S. Krikov, M. L. Feldkamp, E. Lammer, G. M. Shaw; National Birth Defects Prevention Study, Congenital heart defects after maternal fever. *Am. J. Obstet. Gynecol.* **210**, 359.e1–359.e11 (2014).

8. M. E. Oster, T. Riehle-Colarusso, C. J. Alverson, A. Correa, Associations between maternal fever and influenza and congenital heart defects. *J. Pediatr.* **158**, 990–995 (2011).

9. D. W. Smith, S. K. Clarren, M. A. S. Harvey, Hyperthermia as a possible teratogenic agent. *J. Pediatr.* **92**, 878–883 (1978).

10. A. Milunsky, M. Ulcickas, K. J. Rothman, W. Willett, S. S. Jick H. Jick, Maternal heat exposure and neural tube defects. *JAMA* **268**, 882–885 (1992).

11. M. L. Kirby, T. F. Gale, D. E. Stewart, Neural crest cells contribute to normal aorticopulmonary septation. *Science* **220**, 1059–1061 (1983).

12. K. L. Waldo, D. Kumiski, M. L. Kirby, Cardiac neural crest is essential for the persistence rather than the formation of an arch artery. *Dev. Dyn.* **205**, 281–292 (1996).

13. F. Santagati, F. M. Rijli, Cranial neural crest and the building of the vertebrate head. *Nat. Rev. Neurosci.* **4**, 806–818 (2003).

14. A. Keyte, M. R. Hutson, The neural crest in cardiac congenital anomalies. *Differentiation* **84**, 25–40 (2012).

15. L. Leatherbury, H. E. Gauldin, K. Waldo, M. L. Kirby, Microcinephotography of the developing heart in neural crest-ablated chick embryos. *Circulation* **81**, 1047–1057 (1990).

16. Y.-X. Li, M. Zdanowicz, L. Young, D. Kumiski, L. Leatherbury, M. L. Kirby, Cardiac neural crest in zebrafish embryos contributes to myocardial cell lineage and early heart function. *Dev. Dyn.* **226**, 540–550 (2003).

17. K. L. Waldo, M. R. Hutson, C. C. Ward, M. Zdanowicz, H. A. Stadt, D. Kumiski, R. Abu-Issa, M. L. Kirby, Secondary heart field contributes myocardium and smooth muscle to the arterial pole of the developing heart. *Dev. Biol.* **281**, 78–90 (2005).

18. M. J. Caterina, M. A. Schumacher, M. Tominaga, T. A. Rosen, J. D. Levine, D. Julius, The capsaicin receptor: A heat-activated ion channel in the pain pathway. *Nature* **389**, 816–824 (1997).

19. M. J. Caterina, T. A. Rosen, M. Tominaga, A. J. Brake, D. Julius, A capsaicin-receptor homologue with a high threshold for noxious heat. *Nature* **398**, 436–441 (1999).

20. A. Dhaka, A. N. Murray, J. Mathur, T. J. Earley, M. J. Petrus, A. Patapoutian, TRPM8 is required for cold sensation in mice. *Neuron* **54**, 371–378 (2007).

21. J. Waning, J. Vriens, G. Owsianik, L. Stüwe, S. Mally, A. Fabian, C. Frippiat, B. Nilius, A. Schwab, A novel function of capsaicin-sensitive TRPV1 channels: Involvement in cell migration. *Cell Calcium* **42**, 17–25 (2007).

22. E. Martin, D. Dahan, G. Cardouat, J. Gillibert-Duplantier, R. Marthan, J.-P. Savineau, T. Ducret, Involvement of TRPV1 and TRPV4 channels in migration of rat pulmonary arterial smooth muscle cells. *Pflügers Arch.* **464**, 261–272 (2012).

23. L. Ye, S. Kleiner, J. Wu, R. Sah, R. K. Gupta, A. S. Banks, P. Cohen, M. J. Khandekar, P. Boström, R. J. Mepani, D. Laznik, T. M. Kamenecka, X. Song, W. Liedtke, V. K. Mootha, P. Puigserver, P. R. Griffin, D. E. Clapham, B. M. Spiegelman, TRPV4 is a regulator of adipose oxidative metabolism, inflammation, and energy homeostasis. *Cell* **151**, 96–110 (2012).

24. Q. Y. Shi, J. B. Zhang, Y. Q. Mi, Y. Song, J. Ma, Y. L. Zhang, Congenital heart defects and maternal fever: Systematic review and meta-analysis. *J. Perinatol.* **34**, 677–682 (2014).

25. A. D. Güler, H. Lee, T. Iida, I. Shimizu, M. Tominaga, M. Caterina, Heat-evoked activation of the ion channel, TRPV4. *J. Neurosci.* **22**, 6408–6414 (2002).

26. S.-E. Jordt, D. Julius, Molecular basis for species-specific sensitivity to "hot" chili peppers. *Cell* **108**, 421–430 (2002).

27. J. Siemens, S. Zhou, R. Piskorowski, T. Nikai, E. A. Lumpkin, A. I. Basbaum, D. King, D. Julius, Spider toxins activate the capsaicin receptor to produce inflammatory pain. *Nature* **444**, 208–212 (2006).

28. F. Vincent, A. Acevedo, M. T. Nguyen, M. Dourado, J. DeFalco, A. Gustafson, P. Spiro, D. E. Emerling, M. G. Kelly, M. A. J. Duncton, Identification and characterization of novel TRPV4 modulators. *Biochem. Biophys. Res. Commun.* **389**, 490–494 (2009).

29. S. Mangos, Y. Liu, I. A. Drummond, Dynamic expression of the osmosensory channel *trpv4* in multiple developing organs in zebrafish. *Gene Expr. Patterns* **7**, 480–484 (2007).

30. E. Kague, M. Gallagher, S. Burke, M. Parsons, T. Franz-Odendaal, S. Fisher, Skeletogenic fate of zebrafish cranial and trunk neural crest. *PLOS ONE* **7**, e47394 (2012).

31. H. Huang, S. Delikanli, H. Zeng, D. M. Ferkey, A. Pralle, Remote control of ion channels and neurons through magnetic-field heating of nanoparticles. *Nat. Nanotech.* **5**, 602–606 (2010).

32. S. A. Stanley, J. Sauer, R. S. Kane, J. S. Dordick, J. M. Friedman, Remote regulation of glucose homeostasis in mice using genetically encoded nanoparticles. *Nat. Med.* **21**, 92–98 (2015).

33. S. A. Stanley, J. E. Gagner, S. Damanpour, M. Yoshida, J. S. Dordick, J. M. Friedman, Radio-wave heating of iron oxide nanoparticles can regulate plasma glucose in mice. *Science* **336**, 604–608 (2012).

34. M. A. Wheeler, C. J. Smith, M. Ottolini, B. S. Barker, A. M. Purohit, R. M. Grippo, R. P. Gaykema, A. J. Spano, M. P. Beenhakker, S. Kucenas, M. K. Patel, C. D. Deppmann, A. D. Güler, Genetically targeted magnetic control of the nervous system. *Nat. Neurosci.* **19**, 756–761 (2016).

35. L. G. Coffman, D. Parsonage, R. J. D'Agostino Jr., F. M. Torti, S. V. Torti, Regulatory effects of ferritin on angiogenesis. *Proc. Natl. Acad. Sci. U.S.A.* **106**, 570–575 (2009).

36. R. Chen, G. Romero, M. G. Christiansen, A. Mohr, P. Anikeeva, Wireless magnetothermal deep brain stimulation. *Science* **347**, 1477–1480 (2015).

37. J. Grandl, S. E. Kim, V. Uzzell, B. Bursulaya, M. Petrus, A. Bandell, A. Patapoutian, Temperature-induced opening of TRPV1 ion channel is stabilized by the pore domain. *Nat. Neurosci.* **13**, 708–714 (2010).

38. Y. Ishihara, A. Calderon, H. Watanabe, K. Okamoto, Y. Suzuki, K. Kuroda, Y. Suzuki, A precise and fast temperature mapping using water proton chemical shift. *Magn. Reson. Med.* **34**, 814–823 (1995).

39. M. R. Hutson, X. L. Zeng, A. J. Kim, E. Antoon, S. Harward, M. L. Kirby, Arterial pole progenitors interpret opposing FGF/BMP signals to proliferate or differentiate. *Development* **137**, 3001–3011 (2010).

40. M. R. Hutson, P. Zhang, H. A. Stadt, A. K. Sato, Y.-X. Li, J. Burch, T. L. Creazzo, M. L. Kirby, Cardiac arterial pole alignment is sensitive to FGF8 signaling in the pharynx. *Dev. Biol.* **295**, 486–497 (2006).

41. X. Xu, R. Francis, C. J. Wei, K. L. Linask, C. W. Lo, Connexin 43-mediated modulation of polarized cell movement and the directional migration of cardiac neural crest cells. *Development* **133**, 3629–3639 (2006).

42. Y. Liu, Y. Jin, J. Li, E. Seto, E. Kuo, W. Yu, R. J. Schwartz, M. Blazo, S. L. Zhang, X. Peng, Inactivation of Cdc42 in neural crest cells causes craniofacial and cardiovascular morphogenesis defects. *Dev. Biol.* **383**, 239–252 (2013).

43. D. J. Heidenreich, M. V. Reedy, P. R. Brauer, Homocysteine enhances cardiac neural crest cell attachment in vitro by increasing intracellular calcium levels. *Dev. Dyn.* **237**, 2117–2128 (2008).

44. P. R. Brauer, T. H. Rosenquist, Effect of elevated homocysteine on cardiac neural crest migration in vitro. *Dev. Dyn.* **224**, 222–230 (2002).

45. A. Garic, G. R. Flentke, E. Amberger, M. Hernandez, S. M. Smith, CaMKII activation is a novel effector of alcohol's neurotoxicity in neural crest stem/progenitor cells. *J. Neurochem.* **118**, 646–657 (2011).

46. K. V. Ramachandran, J. A. Hennessey, A. S. Barnett, X. Yin, H. A. Stadt, E. Foster, R. A. Shah, M. Yazawa, R. E. Dolmetsch, M. L. Kirby, G. S. Pitt, Calcium influx through L-type $Ca_V1.2$ Ca^{2+} channels regulates mandibular development. *J. Clin. Invest.* **123**, 1638–1646 (2013).

47. C. D. Strader, T. Gaffney, E. E. Sugg, M. R. Candelore, R. Keys, A. A. Patchett, R. A. F. Dixon, Allele-specific activation of genetically engineered receptors. *J. Biol. Chem.* **266**, 5–8 (1991).

48. V. Nawaratne, K. Leach, N. Suratman, R. E. Loiacono, C. C. Felder, B. N. Armbruster, B. L. Roth, P. M. Sexton, A. Christopoulos, New insights into the function of M_4 muscarinic acetylcholine receptors gained using a novel allosteric modulator and a DREADD (designer receptor exclusively activated by a designer drug). *Mol. Pharmacol.* **74**, 1119–1131 (2008).

49. M. Meister, Physical limits to magnetogenetics. *eLife* **5**, e17210 (2016).

50. P. Anikeeva, A. Jasanoff, Problems on the back of an envelope. *eLife* **5**, e19569 (2016).

51. S. A. Stanley, L. Kelly, K. N. Latcha, S. F. Schmidt, X. Yu, A. R. Nectow, J. Sauer, J. P. Dyke, J. S. Dordick, J. M. Friedman, Bidirectional electromagnetic control of the hypothalamus regulates feeding and metabolism. *Nature* **531**, 647–650 (2016).

52. M. J. Edwards, Hyperthermia as a teratogen: A review of experimental studies and their clinical significance. *Teratog. Carcinog. Mutagen.* **6**, 563–582 (1986).

53. M. J. Edwards, Review: Hyperthermia and fever during pregnancy. *Birth Defects Res. A* **76**, 507–516 (2006).

54. P. G. Thorpe, S. M. Gilboa, S. Hernandez-Diaz, J. Lind, J. D. Cragan, G. Briggs, S. Kweder, J. M. Friedman, A. A. Mitchell, M. A. Honein; National Birth Defects Prevention Study, Medications in the first trimester of pregnancy: Most common exposures and critical gaps in understanding fetal risk. *Pharmacoepidemiol. Drug Saf.* **22**, 1013–1018 (2013).

55. M. L. Feldkamp, R. E. Meyer, S. Krikov, L. D. Botto, Acetaminophen use in pregnancy and risk of birth defects: Findings from the National Birth Defects Prevention Study. *Obstet. Gynecol.* **115**, 109–115 (2010).

56. E. Stergiakouli, A. Thapar, G. Davey Smith, Association of acetaminophen use during pregnancy with behavioral problems in childhood: Evidence against confounding. *JAMA Pediatr.* **170**, 964–970 (2016).

57. V. Hamburger, H. L. Hamilton, A series of normal stages in the development of the chick embryo. *J. Morphol.* **88**, 49–92 (1951).

58. G. W. Bell, T. A. Yatskievych, P. B. Antin, GEISHA, a whole-mount in situ hybridization gene expression screen in chicken embryos. *Dev. Dyn.* **229**, 677–687 (2004).

59. C. S. Somogyi, C. Matta, Z. Foldvari, T. Juhász, É. Katona, Á. R. Takács, T. Hajdú, N. Dobrosi, P. Gergely, R. Zákány, Polymodal transient receptor potential vanilloid (TRPV) ion channels in chondrogenic cells. *Int. J. Mol. Sci.* **16**, 18412–18438 (2015).

60. F. Marin, M. A. Nieto, Expression of chicken *slug* and *snail* in mesenchymal components of the developing central nervous system. *Dev. Dyn.* **230**, 144–148 (2004).

61. D. G. Wilkinson, M. A. Nieto, Detection of messenger RNA by in situ hybridization to tissue sections and whole mounts. *Methods Enzymol.* **225**, 361–373 (1993).

62. N. Dib, T. Weller, Two-dimensional finite difference time domain analysis of cylindrical transmission lines. *Int. J. Electron.* **87**, 1065–1081 (2000).

63. J.-P. Berenger, A perfectly matched layer for the absorption of electromagnetic waves. *J. Comput. Phys.* **114**, 185–200 (1994).

64. C. Gabriel, S. Gabriel, E. Corthout, The dielectric properties of biological tissues: I. Literature survey. *Phys. Med. Biol.* **41**, 2231–2249 (1996).

65. T.-W. Chen, T. J. Wardill, Y. Sun, S. R. Pulver, S. L. Renninger, A. Baohan, E. R. Schreiter, R. A. Kerr, M. B. Orger, V. Jayaraman, L. L. Looger, K. Svoboda, D. S. Kim, Ultrasensitive fluorescent proteins for imaging neuronal activity. *Nature* **499**, 295–300 (2013).

66. E. J. Benner, D. Luciano, R. Jo, K. Abdi, P. Paez-Gonzalez, H. Sheng, D. S. Warner, C. Liu, C. Eroglu, C. T. Kuo, Protective astrogenesis from the SVZ niche after injury is controlled by Notch modulator Thbs4. *Nature* **497**, 369–373 (2013).

67. G. A. Johnson, H. Benveniste, R. D. Black, L. W. Hedlund, R. R. Maronpot, B. R. Smith, Histology by magnetic resonance microscopy. *Magn. Reson. Q.* **9**, 1–30 (1993).

68. B. Wu, W. Li, A. V. Avram, S.-M. Gho, C. Liu, Fast and tissue-optimized mapping of magnetic susceptibility and T2* with multi-echo and multi-shot spirals. *Neuroimage* **59**, 297–305 (2012).

69. R. Dibb, Y. Qi, C. Liu, Magnetic susceptibility anisotropy of myocardium imaged by cardiovascular magnetic resonance reflects the anisotropy of myocardial filament α-helix polypeptide bonds. *J. Cardiovasc. Magn. Reson.* **17**, 60 (2015).

70. P. Matak, A. Matak, S. Moustafa, D. K. Aryal, E. J. Benner, W. Wetsel, N. C. Andrews, Disrupted iron homeostasis causes dopaminergic neurodegeneration in mice. *Proc. Natl. Acad. Sci. U.S.A.* **113**, 3428–3435 (2016).

71. R. J. Wassersug, A procedure for differential staining of cartilage and bone in whole formalin-fixed vertebrates. *Stain Technol.* **51**, 131–134 (1976).

72. M. Isrie, M. Breuss, G. Tian, A. H. Hansen, F. Cristofoli, J. Morandell, Z. A. Kupchinsky, A. Sifrim, C. M. Rodriguez-Rodriguez, E. P. Dapena, K. Doonanco, N. Leonard, F. Tinsa, S. Moortgat, H. Ulucan, E. Koparir, E. Karaca, N. Katsanis, V. Marton, J. R. Vermeesch, E. E. Davis, N. J. Cowan, D. A. Keays, H. Van Esch, Mutations in either *TUBB* or *MAPRE2* cause circumferential skin creases kunze type. *A. J. Hum. Genet.* **97**, 790–800 (2015).

73. G. Köntges, A. Lumsden, Rhombencephalic neural crest segmentation is preserved throughout craniofacial ontogeny. *Development* **122**, 3229–3242 (1996).

74. D. M. Noden, The role of the neural crest in patterning of avian cranial skeletal, connective, and muscle tissues. *Dev. Biol.* **96**, 144–165 (1983).

75. G. F. Couly, P. M. Coltey, N. M. Le Douarin, The triple origin of skull in higher vertebrates: A study in quail-chick chimeras. *Development* **117**, 409–429 (1993).

76. N. Wada, Y. Javidan, S. Nelson, T. J. Carney, R. N. Kelsh, T. F. Schilling, Hedgehog signaling is required for cranial neural crest morphogenesis and chondrogenesis at the midline in the zebrafish skull. *Development* **132**, 3977–3988 (2005).

77. N. Ács, F. Bánhidy, E. Puhó, A. E. Czeizel, Maternal influenza during pregnancy and risk of congenital abnormalities in offspring. *Birth Defects Res. A* **73**, 989–996 (2005).

78. M. W. Hentze, M. U. Muckenthaler, B. Galy, C. Camaschella, Two to tango: Regulation of mammalian iron metabolism. *Cell* **142**, 24–38 (2010).

79. K. S. Thorneloe, A. C. Sulpizio, Z. Lin, D. J. Figueroa, A. K. Clouse, G. P. McCafferty, T. P. Chendrimada, E. S. R. Lashinger, E. Gordon, L. Evans, B. A. Misajet, D. J. Demarini, J. H. Nation, L. N. Casillas, R. W. Marquis, B. J. Votta, S. A. Sheardown, X. Xu, D. P. Brooks, N. J. Laping, T. D. Westfall, *N*-((1S)-1-{[4-((2S)-2-{[(2,4-dichlorophenyl)sulfonyl]amino}-3-hydroxypropanoyl)-1-piperazinyl]carbonyl}-3-methylbutyl)-1-benzothiophene-2-carboxamide (GSK1016790A), a novel and potent transient receptor potential vanilloid 4 channel agonist induces urinary bladder contraction and hyperactivity: Part I. *J. Pharmacol. Exp. Ther.* **326**, 432–442 (2008).

Citation: M. R. Hutson, A. L. Keyte, M. Hernández-Morales, E. Gibbs, Z. A. Kupchinsky, I. Argyridis, K. N. Erwin, K. Pegram, M. Kneifel, P. B. Rosenberg, P. Matak, L. Xie, J. Grandl, E. E. Davis, N. Katsanis, C. Liu, E. J. Benner, Temperature-activated ion channels in neural crest cells confer maternal fever–associated birth defects. *Sci. Signal.* **10**, eaal4055 (2017).